How good is the Hadley Centre climate model?
Research at CGAM on identifying and understanding model systematic errors: 1999-2002

Hadley Centre technical notes

Slingo, J. M., E. Guilyardi, K. Hodges, B. J. Hoskins, P. M. Inness, D. M. Lawrence, R. B. Neale, T. M. Osborne, H. Spencer, and G.-Y. Yang.

September 2003

NCAS Centre for Global Atmospheric Modelling

NCAS NERC Centres for Atmospheric Science

How good is the Hadley Centre climate model?

Research at CGAM on identifying and understanding model systematic errors: 1999-2002

Julia Slingo, Eric Guilyardi, Kevin Hodges (ESSC),
Brian Hoskins, Pete Inness, Dave Lawrence, Rich Neale,
Tom Osborne, Hilary Spencer and Gui-Ying Yang

The University of Reading

Contents

Contributors contact details:

Julia Slingo: j.m.slingo@reading.ac.uk
Eric Guilyardi: ericg@met.reading.ac.uk
Kevin Hodges: kih@mail.nerc-essc.ac.uk
Brian Hoskins: b.j.Hoskins@reading.ac.uk
Pete Inness: pete@met.reading.ac.uk
Dave Lawrence: dml@met.reading.ac.uk
Rich Neale: rneale@cdc.noaa.gov
Tom Osborne: swr01tmo@met.reading.ac.uk
Hilary Spencer: swr99hs@met.reading.ac.uk
Gui-Ying Yang: swsyangg@met.reading.ac.uk

1. Introduction

This report provides a synthesis of a wide range of research carried out by CGAM staff over the last three years. In some cases, evidence of model systematic errors arose indirectly from particular research projects and in other cases the research was focused directly on identifying, understanding and improving model errors. For some projects the research is complete and in others, work is continuing to investigate further the model errors and to provide or suggest solutions. The intention is to provide an update to this report every 1 to 2 years.

Climate can be defined in terms of the statistics of the weather at any location and CGAM's approach to understanding model systematic error is often to consider the processes and phenomena acting at synoptic space and time scales. We have found increasing evidence that scale interactions on diurnal to seasonal timescales may be critical for model systematic error and a review of these ideas is provided in Slingo et al. (2003). Increasingly CGAM research involves understanding the role of coupled processes in determining the mean state and variability of the climate system and a theme of this report is the influence of the ocean and the land surface on climate.

As a result of these studies various areas for model development and improvement have been suggested and can be summarised as follows:

- Memory in the convection scheme to provide an evolving convective cloud field, particularly on diurnal timescales.
- Need for tri-modal rather than bi-modal vertical distributions for tropical convection.
- Adequate vertical resolution in the free troposphere to capture the freezing level inversion. A resolution of 50hPa or less is suggested.
- Melting/freezing processes in convective clouds.
- Parametrization of the moistening effects of cumulus congestus clouds, as well as 'warm' rain production.
- Parametrization of the effects of land/sea breezes on convective triggering and sub grid-scale 'gustiness'
- Stochastic forcing of convection by gravity waves, relevant to the self-organisation of convection
- Adequate vertical resolution in the ocean mixed layer to capture the coupling between the atmosphere and upper ocean on diurnal to intraseasonal timescales
- Implementation of seasonally varying vegetation in MOSES-2.
- Improvements to the specification of soil hydraulic parameters to increase model sensitivity to soil moisture variability
- Higher horizontal resolution to represent weather systems (e.g. storm tracks) with greater fidelity and to improve orographic forcing.

Reference:

Slingo, J. M., P. M. Inness, R. B. Neale, S. J. Woolnough and G-Y. Yang, 2003: Scale interactions on diurnal to seasonal timescales and their relevance to model systematic errors. *Annales Geophysicae,* **46**, 139-155.

2. Diurnal and seasonal cycles: Julia Slingo, Gui-Ying Yang

2.1 Diurnal cycle

The diurnal cycle dominates the sub-seasonal variability over tropical and subtropical continents and systematically modifies the precipitation over the tropical oceans (see Yang and Slingo (2001) and references therein). A global, multi-year archive of high-resolution (3 hourly, 0.5^0 latitude/longitude grid) window (11μm) brightness temperature data from multiple satellites has recently been developed by the European Union Cloud Archive User Service (CLAUS) project. It has been used to construct a climatology of the diurnal cycle in convection, cloudiness and surface temperature for all regions of the tropics; this has proved invaluable for assessing the characteristics of the diurnal cycle in HadAM3 (Yang and Slingo 2001).

Figure 2.1 shows the amplitude of the diurnal (24 hours) harmonic in brightness temperature (T_b) and estimated precipitation for northern winter (DJF) and northern summer (JJA), respectively. The maxima in the amplitude of the diurnal cycle in T_b occur over the Atacama and Namib Deserts in DJF and over Saudi Arabia and the Sahara and Kalahari Deserts in JJA. The convective regions over land also show large amplitudes for T_b, consistent with the forcing of convection by the diurnal cycle in land surface heating. This is particularly pronounced over north-east India during the summer monsoon season and demonstrates the importance of the diurnal cycle in modulating monsoon rainfall.

An interesting feature of Figure 2.1 is the spreading of the diurnal amplitude from land convective regions out over the adjacent oceans, suggestive of complex land-sea breeze effects. This is especially marked around the Indonesian Islands in DJF, and over the northern Bay of Bengal and along the central American and Mexican coasts in JJA.

Over the majority of the tropical oceans, the diurnal cycle is much more subtle and is best captured by the estimated precipitation field which focuses on the variations in the cold cloud amounts. The results shown in Figures 2.1(c) and 2.1(d) demonstrate that there is a small but significant diurnal variation in oceanic precipitation of the order of 3-6 $mm.day^{-1}$ along the Intertropical and South Pacific Convergence Zones (ITCZ and SPCZ) in both seasons.

The phase of the diurnal harmonic of brightness temperature and estimated precipitation for DJF and JJA is given in Figure 2.2 in terms of the *local time* of the maximum. Over clear sky land regions, such as the Sahara, the maximum in T_b occurs consistently about 1-2 hours after the peak in the solar heating, indicative of a slight lag in the land surface heating due to the thermal inertia of the soil.

The phase of the diurnal harmonic in the estimated precipitation (Figures 2.2(c) and 2.2(d)), emphasises the timing of the maximum in deep convection. The continental areas show that the maximum in deep convection/precipitation tends to occur in the late afternoon and evening, between 1700 and midnight local time. Over the oceans, the phase of the diurnal cycle is very variable, although for regions of deep convection (characterised by low T_b in Figure 2.1), away from any influence of land forced diurnal variations, the precipitation tends to peak in the early morning, around 0600 local time. However, this result needs to be treated with caution since there are potential inconsistencies between the actual timing of the precipitation maximum and that inferred from the brightness temperature

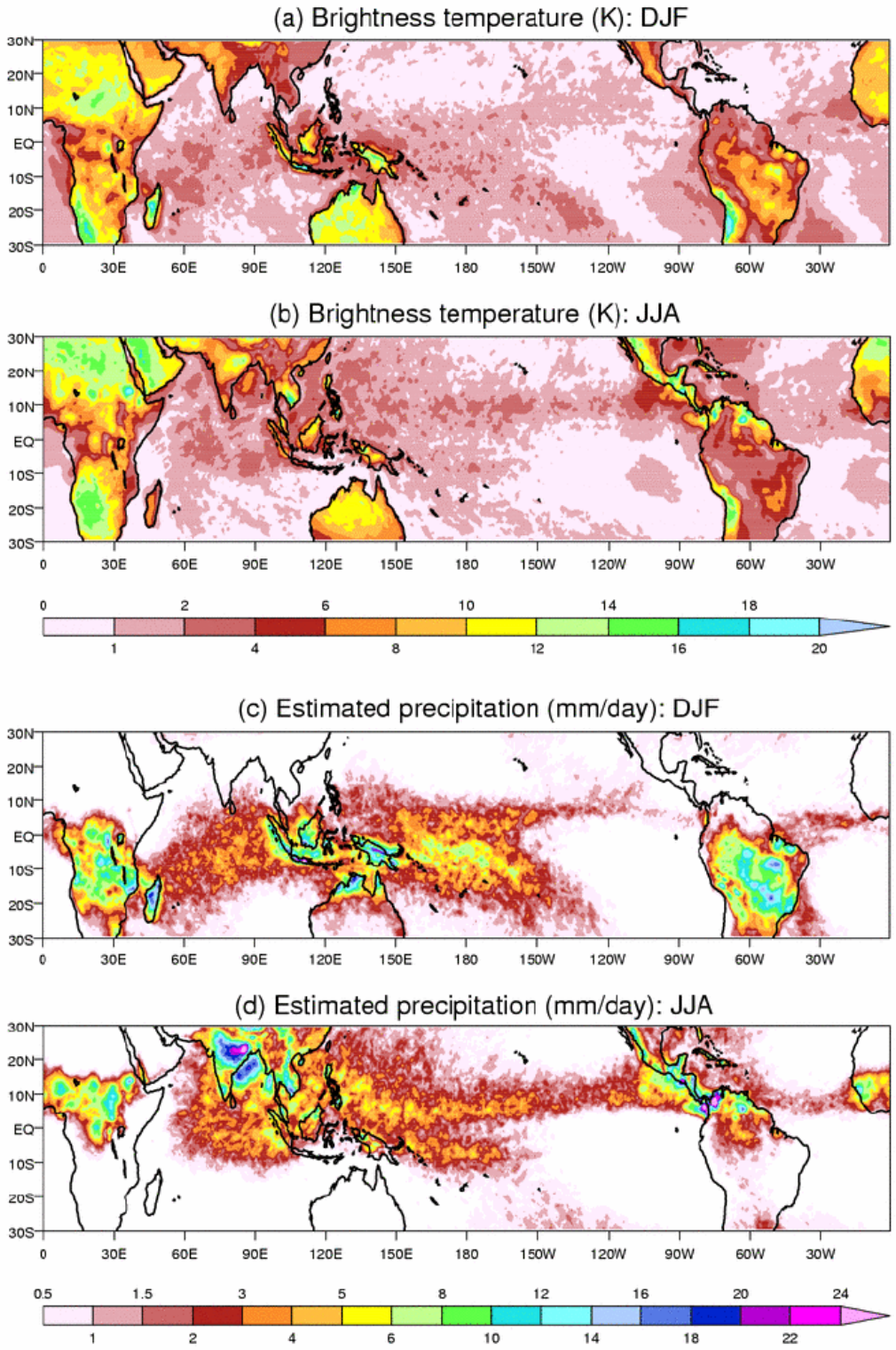

Figure 2.1: Amplitude of the diurnal harmonic in window brightness temperature (T_b) and derived precipitation from the CLAUS data

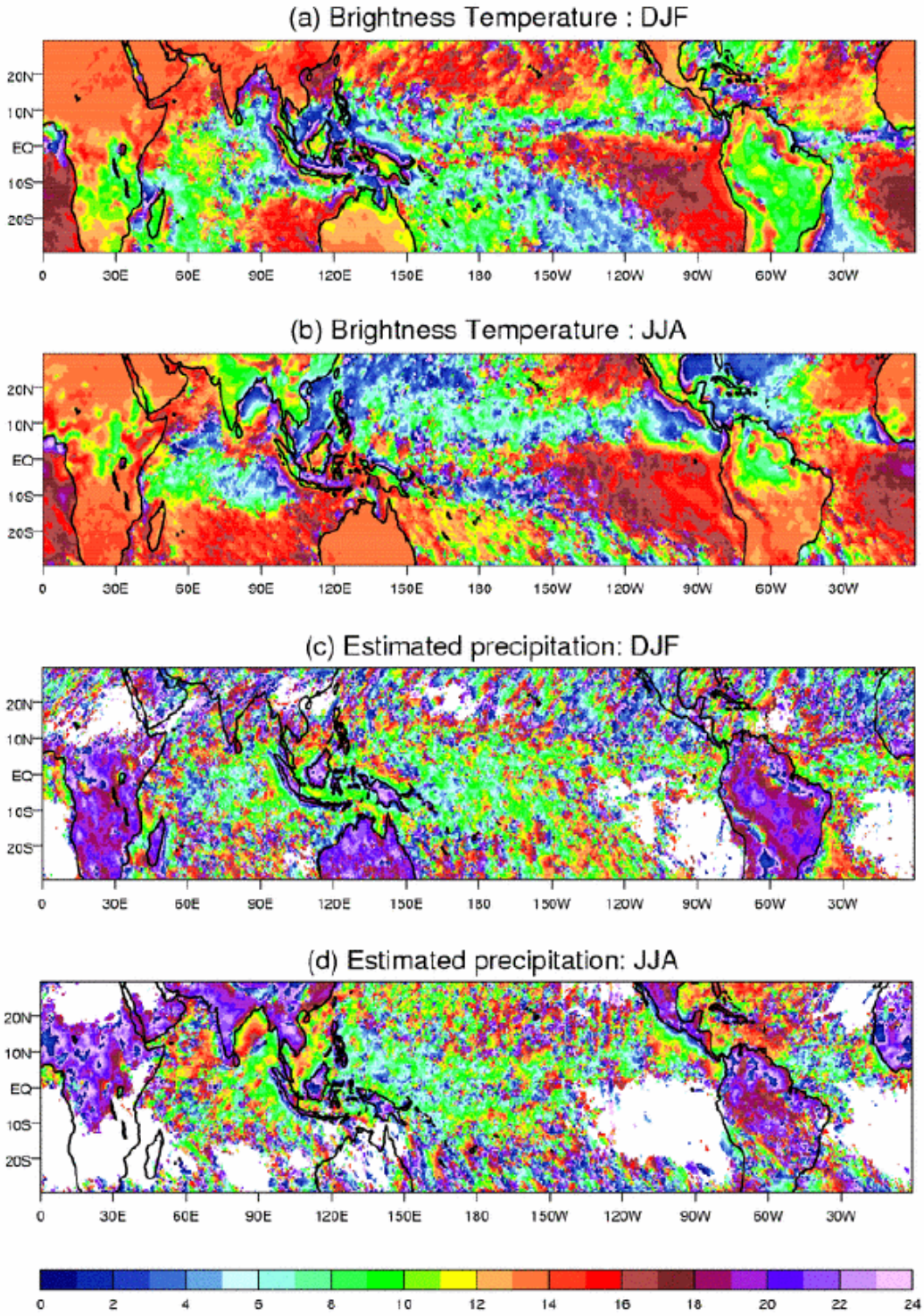

Figure 2.2: Phase (local time of maximum) of the diurnal harmonic in window brightness temperature (T_b) and derived precipitation from the CLAUS data

To provide similar statistics on the diurnal cycle, HadAM3 was integrated for a year with observed SSTs for 1991/92; 3-hourly diagnostics of OLR and precipitation were archived. Versions of the model with 30 (L30) and 19 (L19) vertical levels have been evaluated. Since the results were found to be insensitive to vertical resolution, only those from the L30 version will be presented here.

To allow direct comparison with the CLAUS results, the model's OLR has been converted to an equivalent brightness temperature using the following relationship between the observed window brightness temperature (T_b) and the flux equivalent brightness temperature (T_f), as proposed by Ohring and Gruber (1984):

$$T_f = T_b.(a + b.\ T_b)$$

where a=1.228 and b=$-1.106*10^{-3}$ K^{-1}. Then T_f is related to OLR by:

$$OLR = \sigma.\ T_f^{\ 4}$$

The amplitudes of the diurnal harmonic in the simulated equivalent T_b and precipitation for DJF and JJA are shown in Figure 2.3. In comparison with the results from CLAUS (Figure 2.1), the model has successfully simulated many aspects of the amplitude of the diurnal harmonic. The spatial patterns are slightly different which may be associated partly with systematic errors in the model's basic climate, and partly with the limited sample size. The amplitudes of the diurnal harmonic in equivalent T_b are generally well captured over the clear sky land areas of North Africa, but are underestimated for Australia, particularly during southern winter.

The diurnal amplitude in precipitation over continental convective regions, such as South Africa in DJF and central Africa in JJA, is generally well captured. Obvious discrepancies are over the islands of the maritime continent in DJF, and over the Indian monsoon region in JJA. The model has failed to capture the pronounced diurnal cycle over northern India, but has simulated rather large amplitudes in equivalent T_b over the Arabian Sea and Bay of Bengal that are not co-located with those in precipitation, nor seen in the CLAUS results. Over the open oceans, the model appears to have slightly overestimated the amplitude of the diurnal harmonic in equivalent T_b but underestimated it in precipitation, although the limitations of the CLAUS results should be noted.

In comparison with the CLAUS results, HadAM3 simulates poorly the phase of the diurnal cycle of precipitation in the tropics (Figure 2.4). The most marked discrepancy occurs for land convective regimes where the diurnal maximum in the simulated precipitation occurs before noon, instead of in the late afternoon and evening as indicated in the CLAUS data. The model also advances the timing of the simulated diurnal maximum in oceanic deep convection by several hours. Over land clear sky regions, the model gives a maximum in T_b coincident with the peak in solar heating, 1-2 hours earlier than that observed in the CLAUS data. However, it has been shown that this error is largely due to the technical implementation of the radiation scheme in which full radiation calculations are only performed every 3 hours (Yang and Slingo 2001).

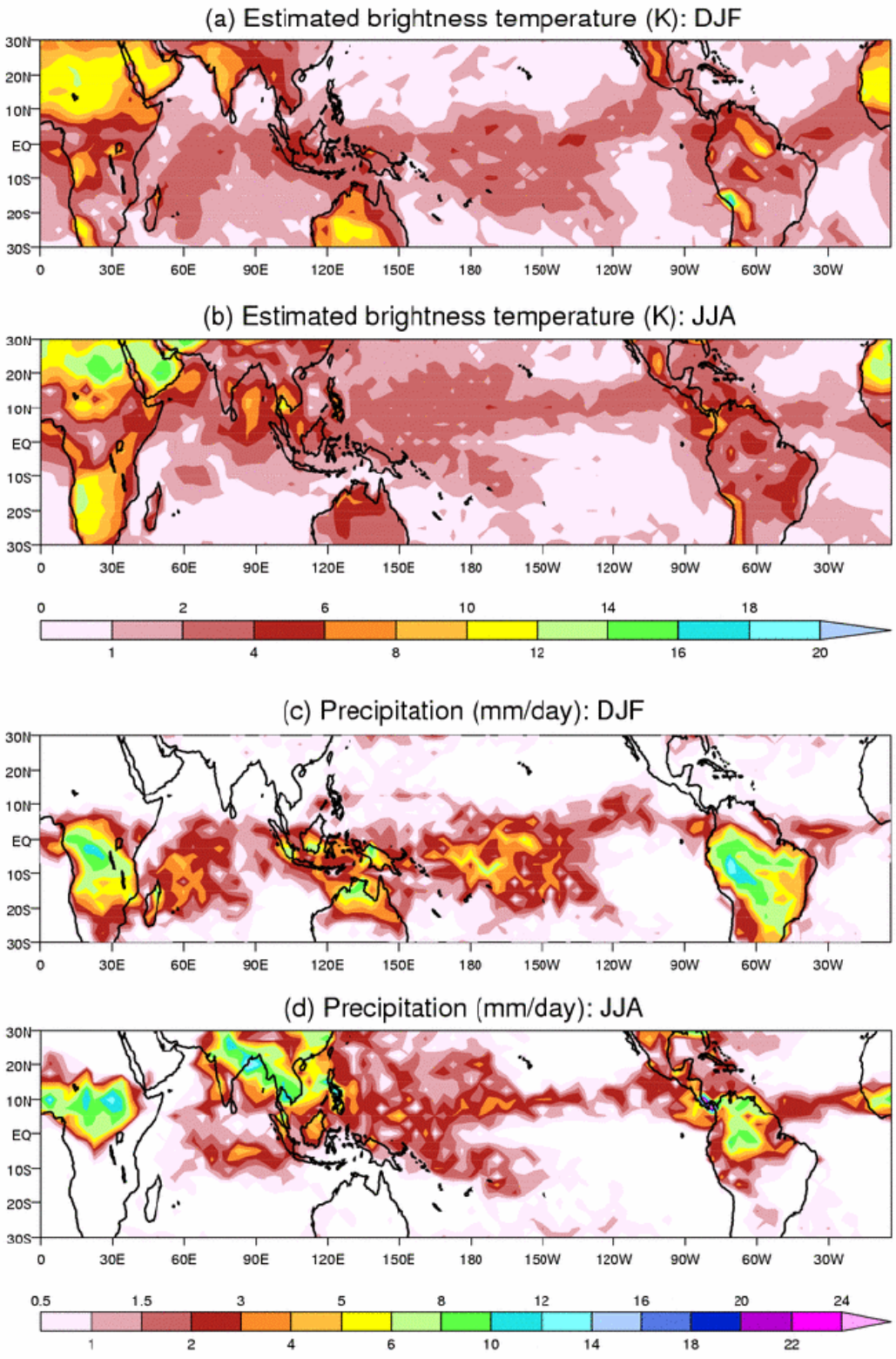

Figure 2.3: Amplitude of the diurnal harmonic in estimated window brightness temperature (T_b) and precipitation from HadAM3

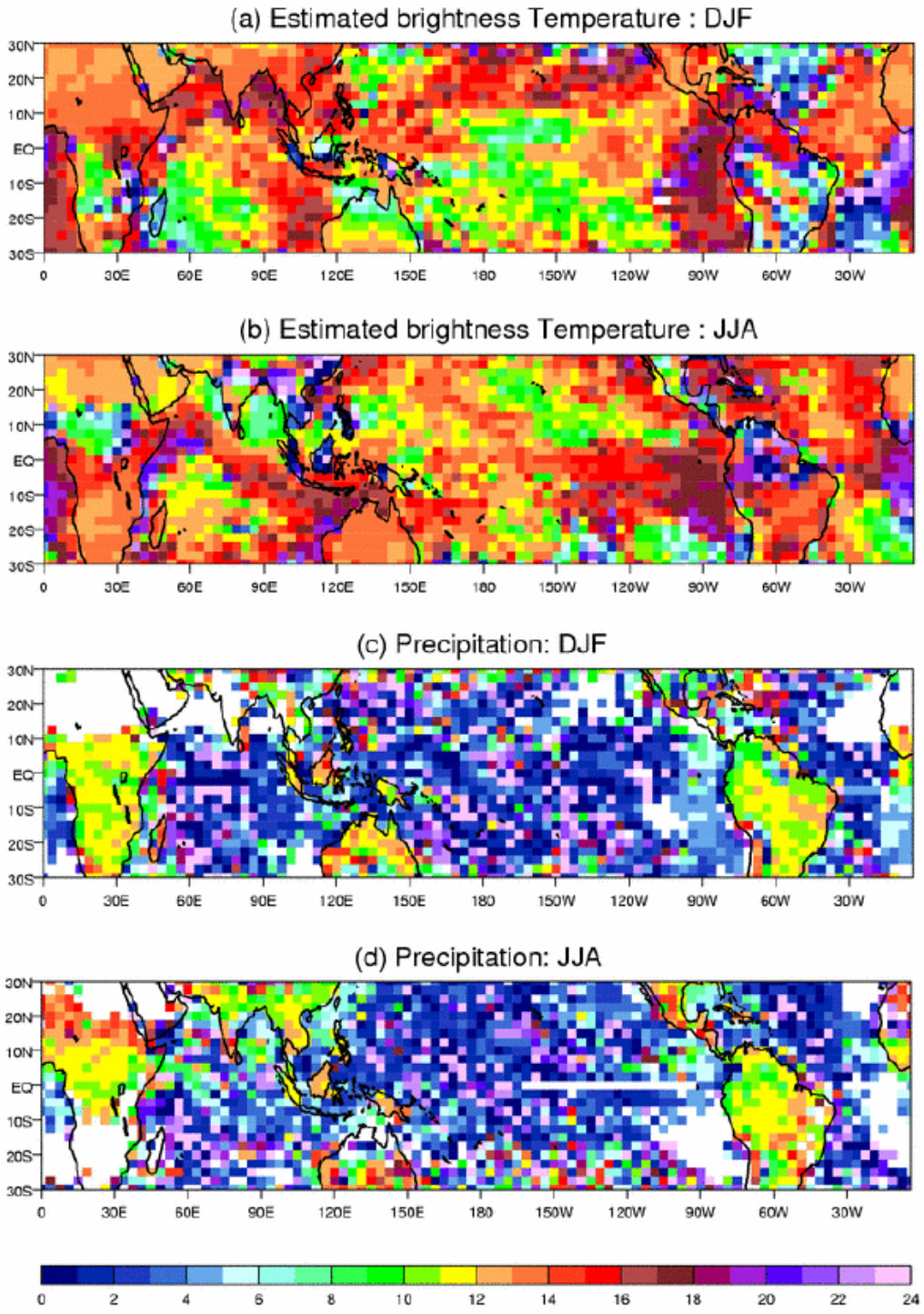

Figure 2.3: Phase (local time of maximum) of the diurnal harmonic in estimated window brightness temperature (T_b) and precipitation from HadAM3

2.2 Seasonal cycle

For the extra-tropics and monsoon regimes, the seasonal cycle represents a dominant climatic fluctuation. The ability of current climate models to simulate the seasonal cycle has been investigated in terms of the amplitude and phase of the 2 metre air temperature (T_{air}) and total precipitation (P). These were chosen because they are key variables for climate change scenarios, and because land-sea temperature contrasts

drive monsoon circulations so that a strong link exists between the seasonal cycle in T_{air} and in P.

Figure 2.5 shows the amplitude and month of maximum/minimum in the seasonal cycle of T_{air} from the climatology of Legates and Willmott (note that very similar results are obtained from the ERA-15 climatology).

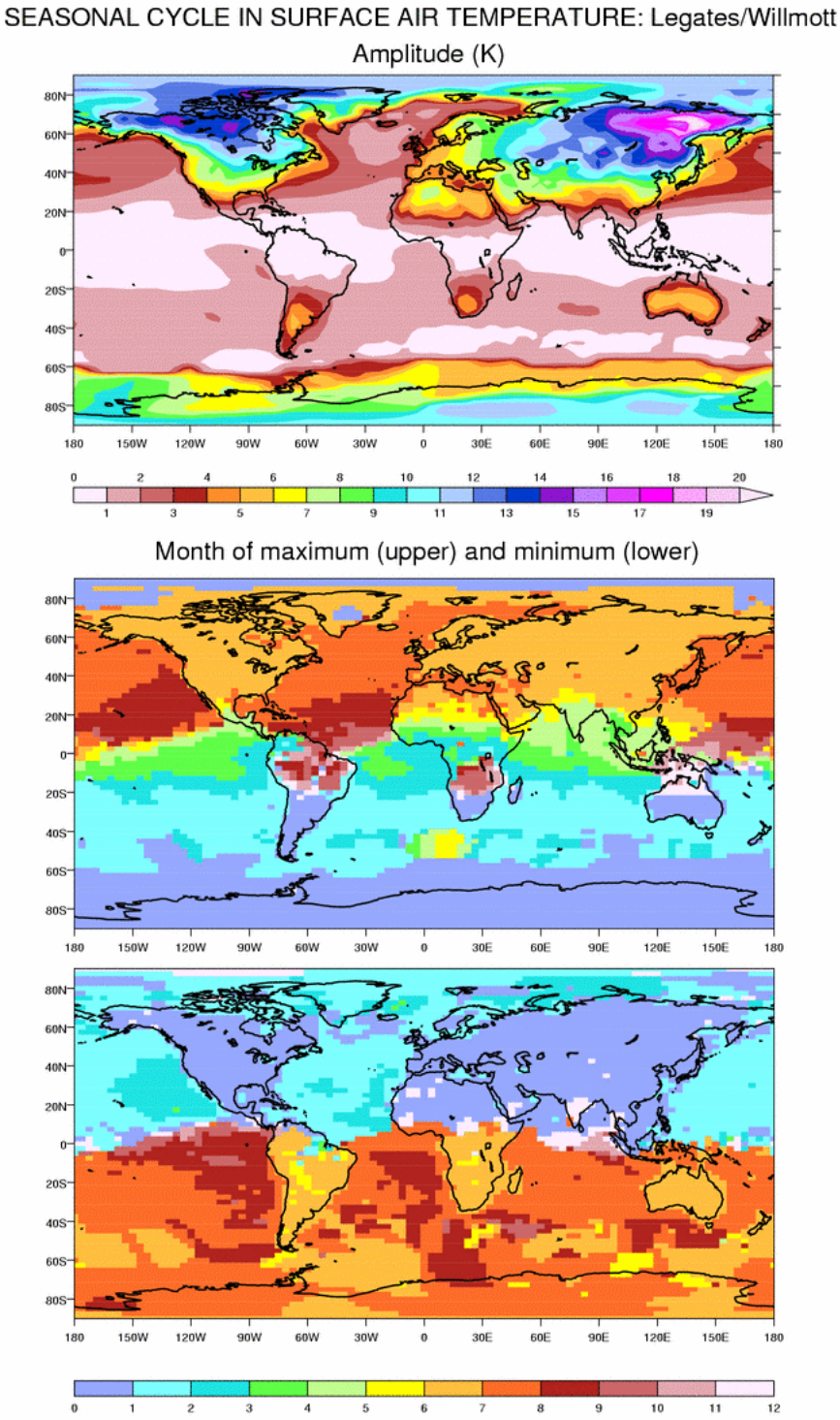

Figure 2.5: Amplitude and month of Maximum/Minimum in the seasonal cycle of surface air temperature from the climatology of Legates and Willmott.

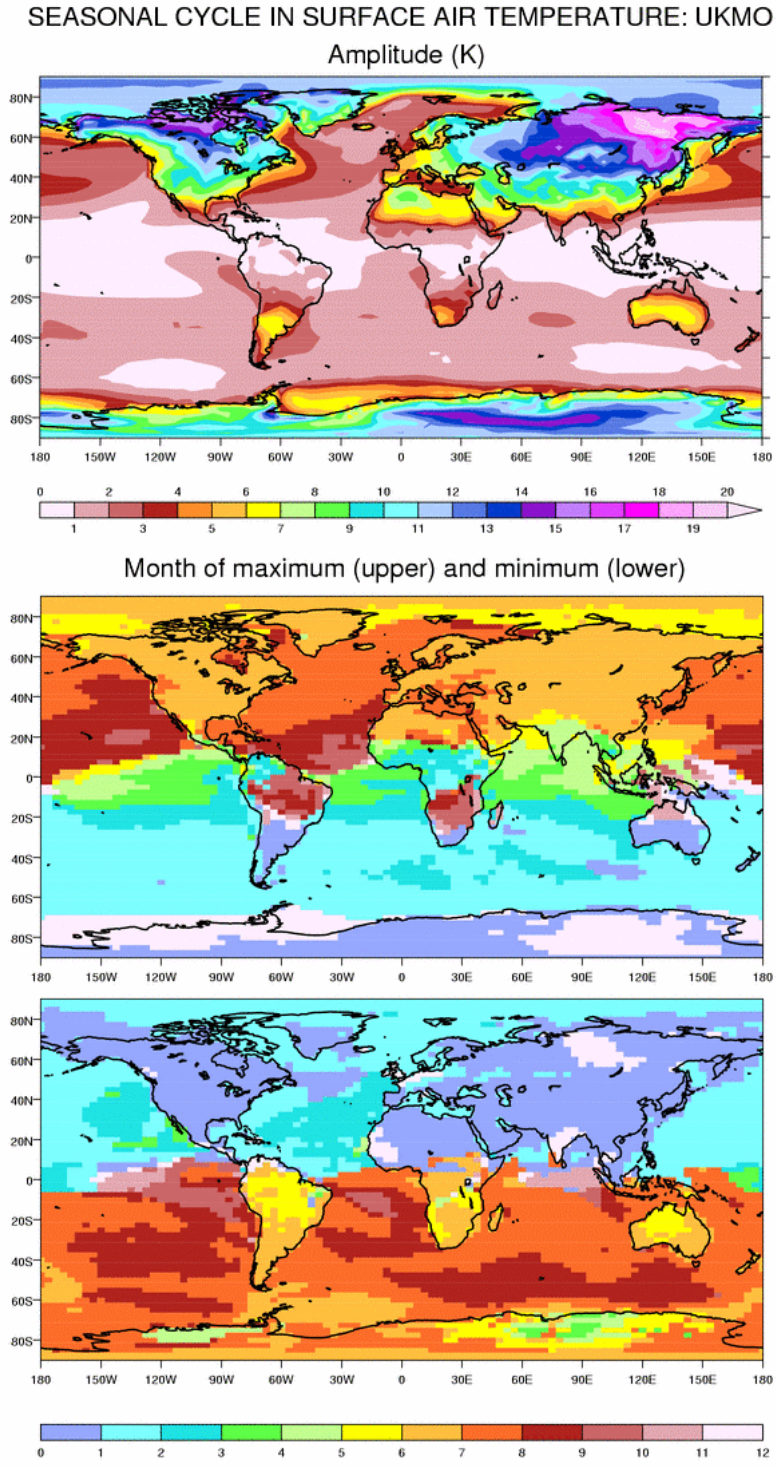

Figure 2.6: Amplitude and month of Maximum/Minimum in the seasonal cycle of surface air temperature from HadAM3 AMIP II simulation.

The results from HadAM3 (Figure 2.6) show that the model captures the maximum amplitude in the seasonal cycle of T_{air} over the eastern portions of the northern hemisphere extra-tropical continents, away from the moderating effects of the oceans. Over the extra-tropical continents, the timing of the maximum and minimum in T_{air},

typically in the month following the solstice, is generally well captured. In the tropics and subtropics, however, the phase of the seasonal cycle is dominated by the progression of the monsoons, with maxima in T_{air} typically occurring in spring before the beginning of the rainy season. Here HadAM3 is less successful, reflecting difficulties in simulating the timing of the onset of the monsoon, particularly over West Africa.

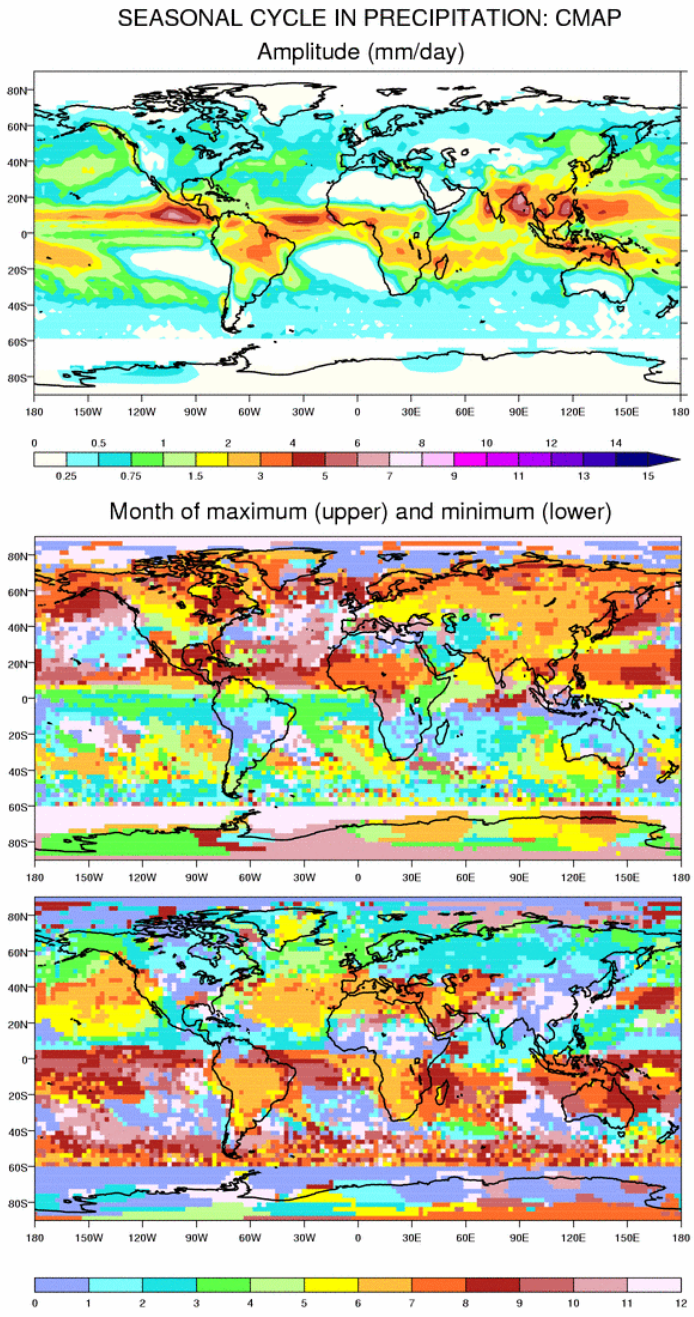

Figure 2.7: Amplitude and month of Maximum/Minimum in the seasonal cycle of precipitation from the CMAP climatology.

The seasonal cycle in precipitation (P) is dominated by transitions of the monsoons and the ITCZ (Figure 2.7). Unlike T_{air}, the maximum amplitudes occur in the tropics and subtropics. In the extra-tropics the largest seasonal cycle in precipitation occurs

along the western coast of N. America and Canada. Globally, the maximum in P typically occurs in the three months following the summer solstice, the exception being the western seaboards of the northern hemisphere continents where the rainfall is most strongly influenced by the seasonality of the storm tracks. The other interesting exception is the Mediterranean and the Middle East where the remote effects of the Asian Summer Monsoon serve to suppress convection and give rise to dry summers.

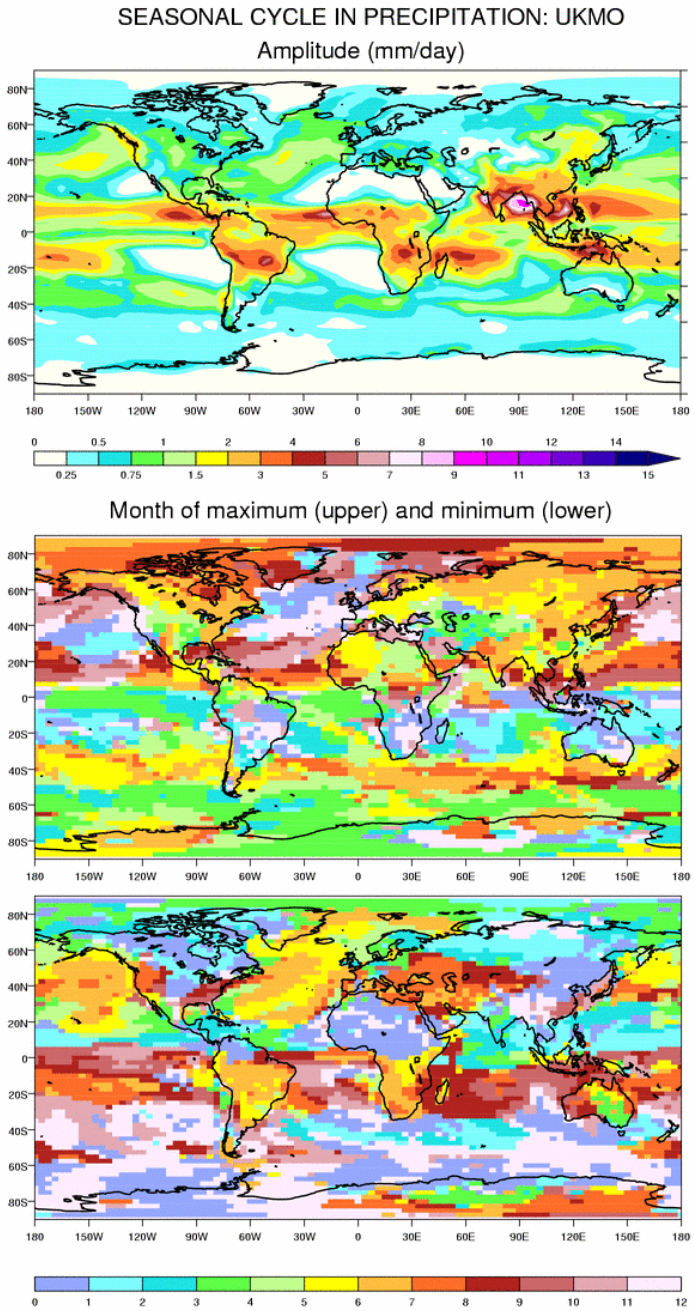

Figure 2.8: Amplitude and month of Maximum/Minimum in the seasonal cycle of precipitation from HadAM3 AMIP II simulation.

The simulation of the seasonal cycle in precipitation by HadAM3 (Figure 2.8) is generally less successful than for T_{air}. Although HadAM3 captures the timing of the

monsoon transitions, particularly over S.E Asia, the patterns and strength of the seasonal cycle are much more variable. As noted earlier, the West African Monsoon penetrates too far north and arrives too early in HadAM3.

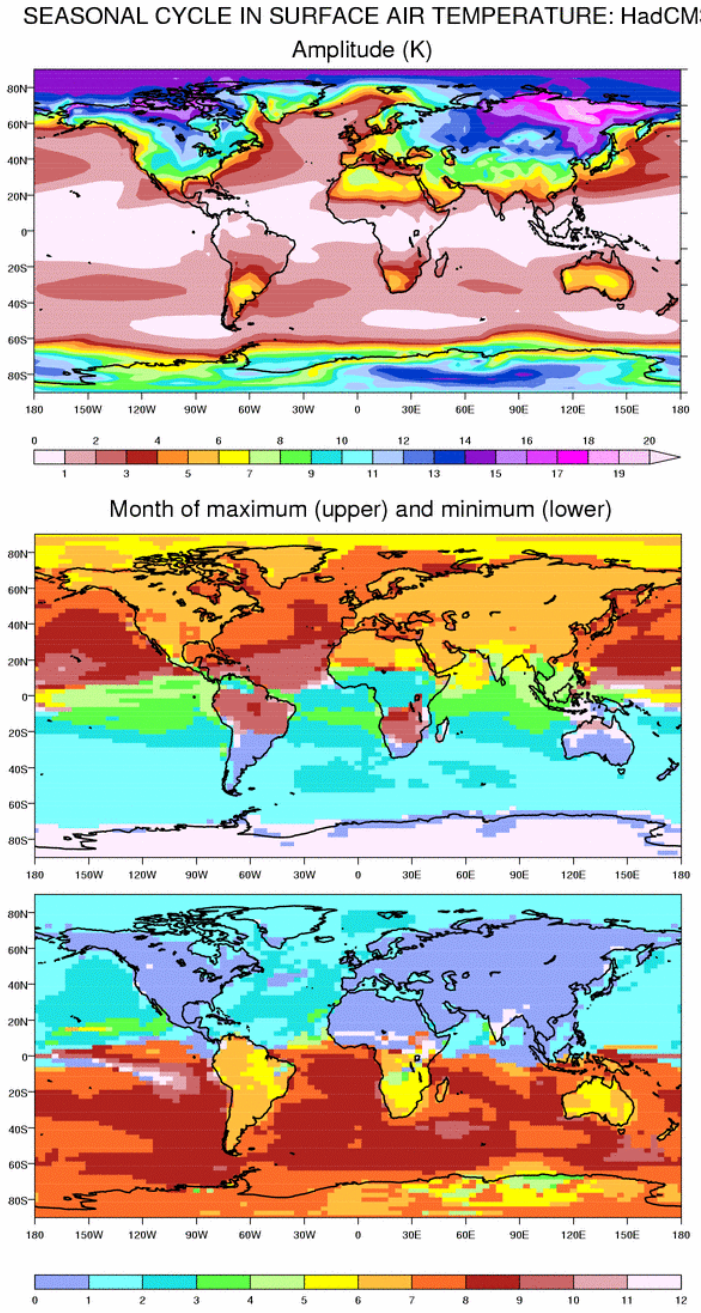

Figure 2.9: Amplitude and month of Maximum/Minimum in the seasonal cycle of surface air temperature from HadCM3.

It is interesting to note that the seasonal cycle in T_{air} (Figure 2.9) and precipitation (not shown) in the coupled model (HadCM3) shows similar characteristics to the uncoupled version (HadAM3), suggesting that the land surface temperatures are the major controlling factor. This is despite the tendency for the phase of the seasonal cycle in the simulated SSTs to be about 1 month later than the observed SSTs,

suggesting perhaps that the thermal inertia of the upper layers of the ocean is too great.

References:

Ohring, G. and A. Gruber, 1984: Satellite determination of the relationship between total longwave radiation flux and infrared window radiance. *J. Clim. Appl. Met.*, **23**, 416-425.

Yang, G-Y. and J. M. Slingo, 2001: The diurnal cycle in the tropics. *Mon. Weath. Rev.*, **129**, 784-801.

3. Convectively coupled equatorial waves in standard and high resolution runs of the HadAM3: Gui-Ying Yang, Brian Hoskins and Julia Slingo

3.*1. Introduction*

Convectively coupled equatorial waves are fundamental components of the complete picture of the tropical atmosphere that involve the interactions of convection and other physical processes with each other and with the dynamics. A faithful representation of these interactions and wave modes is needed for predictions on all time-scales. However, at present there is little understanding of how well they are treated in state-of-the-art models and knowledge of these waves is very limited.

To increase the understanding of the large-scale interaction of physics and dynamics in the tropical atmosphere in the context of the coupled behaviour of equatorial wave motions and deep convection, and to use that understanding to provide the basis for improving the representation of these interactions in climate and weather models, satellite observed window brightness temperature data (T_b, from the EU CLAUS Project; website) and the ERA 15 data have been used to diagnose the coupled large-scale wave motions and deep convection that occur in the tropical atmosphere (Yang et al. 2003). The results have been used as validation of the ability of standard (N48) and high resolution (N144) AMIP II simulations with the HadAM3 in representing the equatorial wave modes and their coupled behaviour.

2. Temporal and spatial variability of tropical convection

As a preliminary study, space-time spectral analysis has been performed on the observed (CLAUS) T_b and the outgoing longwave radiation (OLR) from the HadAM3 standard resolution (SRES; N48) AMIPII (1979-95) integration. Figure 3.1 (left panels) shows the space-time spectra, averaged between 20^oN and 20^oS for the summer (May to October) of 1992 from the CLAUS T_b data. The background red spectrum has been removed (following Wheeler and Kiladis 1999), to emphasise the preferred space and timescales of tropical convection, and the theoretical dispersion curves for equatorial wave modes are included for a range of typical equivalent depths. Figure 3.1 clearly demonstrates that observed tropical convection is organised on preferred space and time scales which coincide with various theoretical equatorial waves modes (inertio-gravity (IG), equatorial Rossby (R), mixed Rossby-gravity (MRG) and Kelvin (K) waves).

In comparison, a similar analysis of model OLR in the SRES AMIP2 simulation (Figure 3.1; middle panels) shows that it contains very limited variance coincident with these equatorial wave modes. Even allowing for possible deficiencies in the model's OLR associated with known difficulties in linking convection with high level cloudiness, it is clear that convectively coupled equatorial waves are almost entirely absent from the model. A similar analysis was also performed on precipitation and vertical motion at 500hPa to confirm that the lack of wave activity was not an artefact of problems with the OLR field. Although there was slightly more evidence of K-waves in the vertical motion field, the overall conclusion on wave activity still stands.

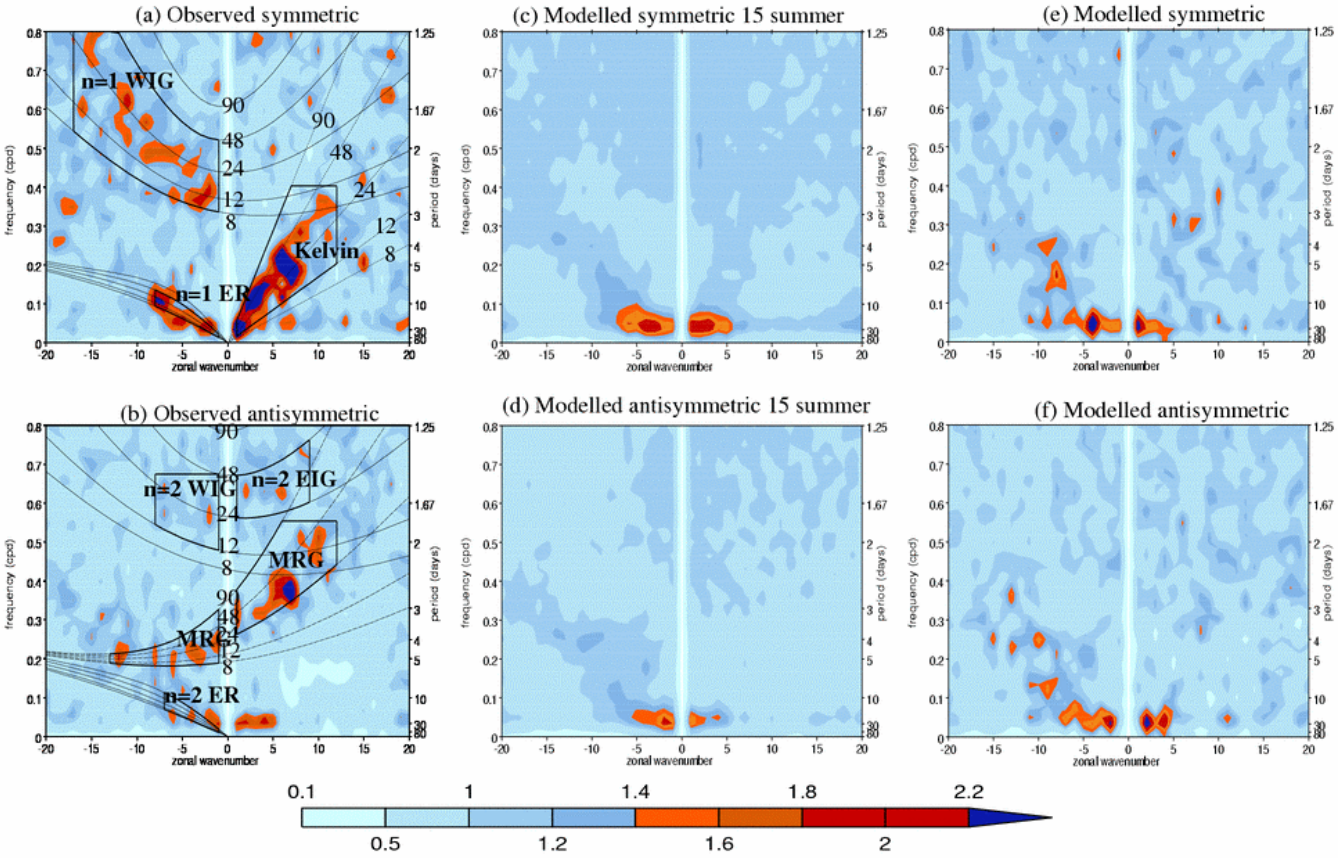

Figure 3.1. Zonal wavenumber-frequency power spectra divided by background power of the (a) symmetric (the odd meridional mode number n) and (b) antisymmetric (even n) components of CLAUS brightness temperature (T_b) for 1992 summer (May-October). The monthly mean has been removed from the field and the power has been averaged over the latitudes 20°N-20°S. (c) and (d) as in (a) and (b) but for OLR from the standard resolution (SRES) AMIP II integration with HadAM3 for 15 summer mean, averaged over 15°N-15°S. (e) and (f) as in (a) and (b) but for high resolution (HRES) AMIP II integration for 1992 summer. Superimposed thin lines in (a) and (b) are the dispersion curves of the odd and even n equatorial waves for the equivalent depths of h=8, 12, 24, 48 and 90m. The curves have been Doppler-shifted with a 3 ms^{-1} easterly basic state.

To investigate if the lack of convectively coupled equatorial waves is associated with model resolution, a similar analysis was performed on a high-resolution run of HadAM3 (HRES; N144 - 1.25°*0.833°) for May-October 1992. Figure 3.1 (right panels) shows that there is little improvement with the move to higher resolution. The spectra show some westward moving variance associated with Rossby and WMRG waves, but lacks variance associated with the Kelvin, eastward EMRG and westward moving *n*=1 gravity waves.

For a more quantitative comparison, model OLR is converted to window brightness temperature using the formula $OLR=\sigma T_f^4$, where $T_f = T_b(a+bT_b)$ is the flux equivalent brightness temperature, and $a=1.228$ and $b=-1.106*10^{-3}\ K^{-1}$ (see Ohring and Gruber 1984). Comparison of the total, eastward and westward moving variance in T_b for the typical space-time domain of most equatorial waves (zonal wavenumber k = ±2 to

±10, period 3 to 30 days), shows that the model generally simulates reasonable off-equatorial (5^o-20^o) convective variability but much less variability in the near equatorial region (5^oN-5^oS), especially for the eastward moving, equatorially-centred convection in the western Pacific region. Averaged over the whole equatorial strip (5^oN-5^oS) the model variance is about 39% and 65% of that of observed for eastward and westward moving disturbances, respectively.

3.3. Identification of equatorial wave structures and their convectively coupled features.

The comprehensive study of observed convectively coupled equatorial waves, described in Yang et al. (2003), has shown that the spectral analysis technique is not sufficient for isolating various equatorial wave modes where the background state winds are variable and the waves are subject to varying degrees of Doppler shifting. A new methodology, which isolates individual equatorial modes based on theoretical structures, has been developed and applied to two independent data sources, ERA 15 and CLAUS T_b data for the summer (May-October) of 1992 (Yang et al. 2003). Various convectively coupled equatorial Kelvin, MRG and Rossby waves, have been detected with a robust consistency between the two independent data sources. The analysis method works well and the gap between basic analytical theory and real complex atmospheric behaviour has been successfully bridged. This method provides a powerful diagnostic tool for investigating convectively coupled equatorial waves and the interaction of equatorial dynamics and physics in the atmosphere, and has enabled some key questions concerning the interaction between dynamics and convection to be addressed.

The methodology is based on the horizontal structures for the gravest equatorial wave modes (Figure 3.2) provided by wave theory. These are used to project upper and lower tropospheric height and wind data on to equatorial wave modes. If the low-level convergence and upper level divergence in the first internal mode, with associated mid-tropospheric ascent, provide the organization for convection, then we would expect this convection to occur in the blue-green shaded regions in Fig. 3.2, which are off-equatorial for the WMRG and R1 waves and centred on the equator for the Kelvin wave.

In addition, Yang et al. (2003) have suggested that wind-dependent surface fluxes of moist entropy may play an important organizational role for convection, particularly where the SSTs are sufficiently warm to support convection. Such conditions potentially occur in the Kelvin and R1 waves, which have maximum zonal winds on the equator shown as the blue and red ovals in Fig. 3.2. Whether the convection would coincide with the blue or red oval would depend on the sign and magnitude of the background zonal wind. In the Kelvin wave, this translates into a spatial shift of the convection away from the low-level convergence maximum.

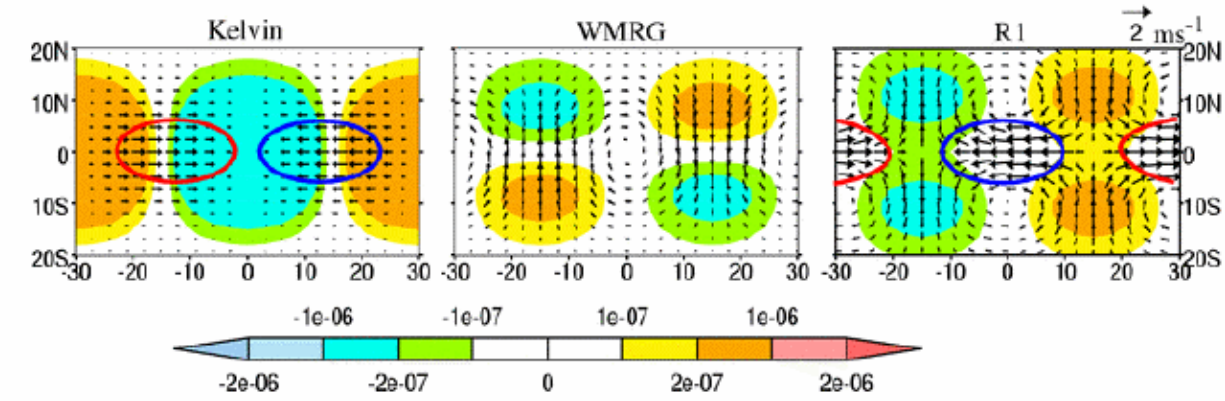

Figure 3.2. Dimensional horizontal wind (vector) and divergence (colour) solutions of the theoretical equatorially trapped Kelvin wave with zonal wind $u_oD_o(y/y_o)\ e^{i(kx-\omega t)}$; n=0 westward mixed Rossby-gravity (WMRG) and the n=1 Rossby (R1) waves with meridional wind $v_nD_n(y/y_o)\ e^{i(kx-\omega t)}$, where n is the meridional mode number, $u_o=v_n=1ms^{-1}$, D_n is a parabolic cylinder function, and the trapping scale $y_o=6^o$ and zonal wave number k=6. Values for y_o and k are chosen based on an analysis of observation data in Yang et al. (2003) for the convenience of comparison. Units are ms^{-1} for wind and s^{-1} for divergence. Colour circles for Kelvin and Rossby waves indicate the possible regions of convection induced by wind-dependent surface energy fluxes.

Application of the method to the CLAUS T_b and ERA-15 data has shown that much of the organised convection in the tropics can be associated with theoretical equatorial Kelvin, MRG and Rossby waves. The characteristics (vertical structure, phase speed) of convectively coupled equatorial waves differ significantly for the various wave modes, and for different hemispheres (i.e. dependent on SST and background winds) and time periods (early/late summer versus mid-summer). Coupling features also vary between off-equatorial and equatorial centred convection. Lower tropospheric waves coupled with off-equatorial convection are generally consistent with those predicted by equatorial wave theory, with convergence/divergence (coincident with southerly/northerly winds in the northern hemisphere) closely connected with intensified/suppressed convection.

The westward, coupled MRG waves show the best consistency with the theory, with a well-defined first internal mode structure (Fig. 3.3, left panels). However, westward moving equatorial *n*=1 Rossby waves (R1) only show the first internal mode structure in the eastern hemisphere (not shown), and tend to be dominated by a barotropic structure in the western hemisphere (Fig. 3.4, left panels).

Whether the waves are significantly coupled with convection and what the wavelength of these coupled modes might be, can be deduced from the regression t-value (regression slope normalized by its standard error) between maxima in convection (from T_b) and the appropriate wind field. For the WMRG waves, the coupling with convection is strong particularly in the up-stream direction. The coupled wavelength is typically between 45^o and 60^o, as estimated from successive peaks, and significant coupling can occur at least at one wavelength. The regression of the convective maxima on to the wind fields (Figures 3.3 and 3.4, lower panels) describes the basic dynamical structures associated with convectively coupled waves.

These structures can be compared with the theoretical description given in Figure 3.2, thus providing an indication of how convective coupling can modify the structure of the waves.

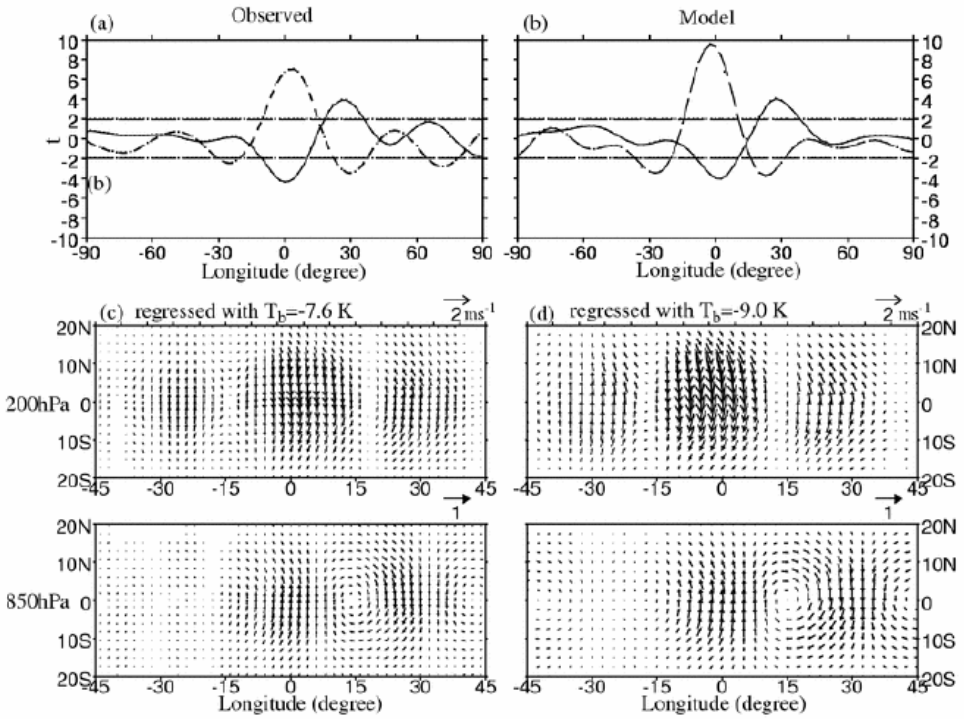

Figure 3.3. Seasonal statistical analysis of westward moving convectively coupled WMRG wave, observed (left panels) and modeled (right panels) in the eastern hemisphere. (a)-(b): Strength of the relationship between off-equatorial convection (T_b extrema at 6^oN-16^oN) and meridional winds (v; 850hPa solid line, 200hPa dotted line) at the equator of the WMRG wave, expressed by the t-value (the linear regression slope divided by its standard error) as a function of longitude. Positive (negative) longitude indicates v field to the east (west) of convective maximum, notionally located at 0^o longitude. Note that the v extrema are coincident with the divergent and convergent centers as shown in the theory (Fig.2) so that the v fields should be correlated with convection. Two straight dashed lines indicate the t-value with 95% confident interval. (c)-(d): Corresponding horizontal winds of the MRG wave regressed with T_b = -7.6K and -9.0K at 0^o longitude for the observations and model data, respectively. The two T_b values are 1.5 times of their peak standard deviation in the eastern hemisphere, 6^oN-16^oN. Unit for winds is ms^{-1}.

The potential for equatorial convection to be influenced by wind-induced surface fluxes of moist entropy has already been noted. There is good evidence from the observations that this does indeed occur, especially over the warm SSTs of the eastern hemisphere. For the Kelvin wave (Fig. 3.5, left panels), there is a closer association between convection and lower tropospheric anomalous zonal winds, than with the lower tropospheric convergence expected from theory (Figure 3.2). This leads to a westwards tilt with height, with the upper level divergence being more closely associated with convection.

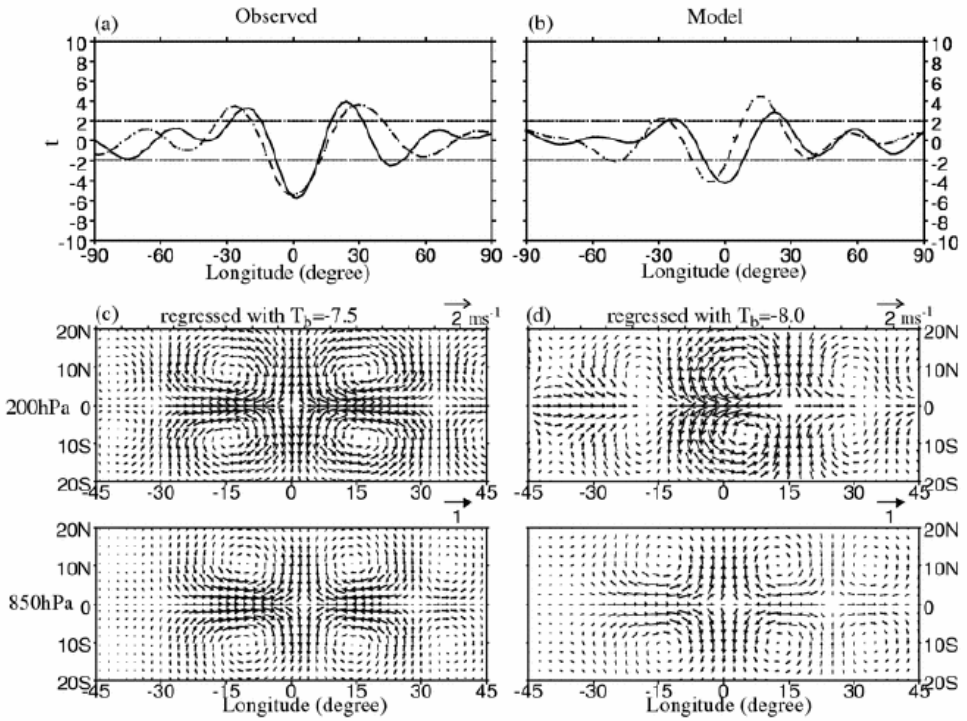

Fig.3.4. As in Fig.3.3 but for the westward moving R1 wave associated with off-equatorial convection (T_b at 8^oN-18^oN) and meridional winds at 8^oN in the western hemisphere.

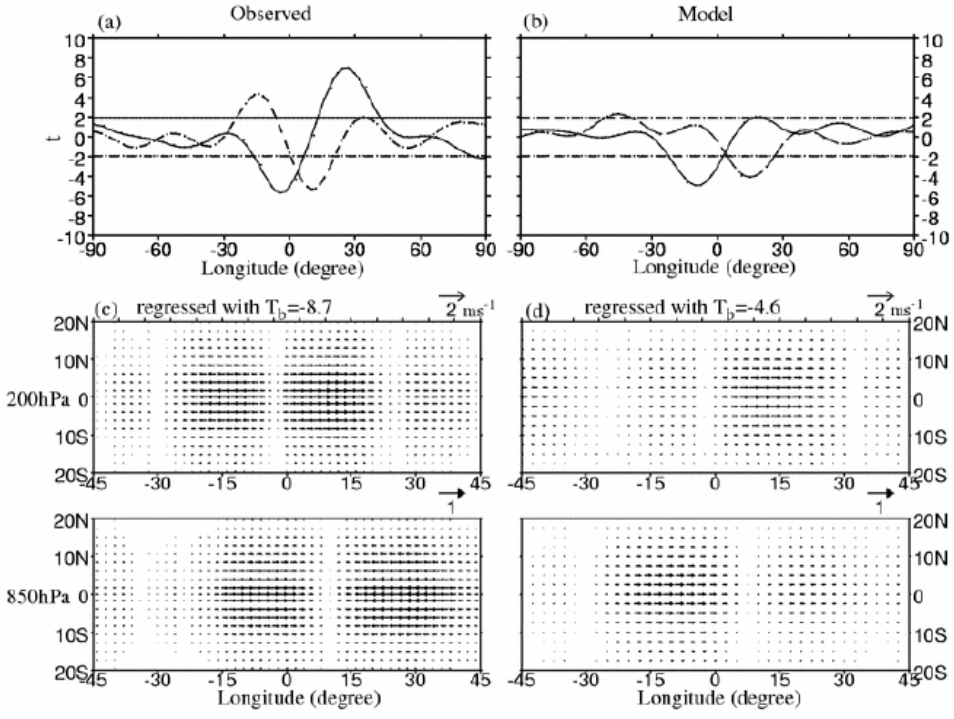

Figure 3.5. As in Fig.3.3 but for the eastward moving Kelvin wave associated with equatorial convection (T_b at 5^oN-5^oS) in the eastern hemisphere. (a)-(b) t-value of the relationship between the Kelvin wave (u at the equator) and the convection. (c)-(d) horizontal winds of the Kelvin wave regressed against the convective maxima.

A similar association between equatorial convection and anomalous zonal winds has also been found for the n=1 Rossby (R1) wave, particularly for westward moving equatorial convection in the eastern hemisphere (Figure 3.6, left panels). The probability distribution function (PDF) of the equatorial convection versus the anomalous zonal winds shows that enhanced convection is closely related to westerly winds for the wave, consistent with the red oval in Figure 3.2 and in line with the mean low level westerly background state in the eastern hemisphere. This convective response to the anomalous equatorial zonal winds modifies the structure of the R1 wave so that it no longer closely resembles its theoretical counterpart. In particular, the equatorial westerly wind anomalies are considerably strengthened (Figure 3.6) by a positive feedback between convection and the wind field. Based on the above results it seems that some equatorial modes can act as the forcing agent of convection, and that convection itself can modify the structure of some of the theoretical modes through a feedback between the winds and the convection.

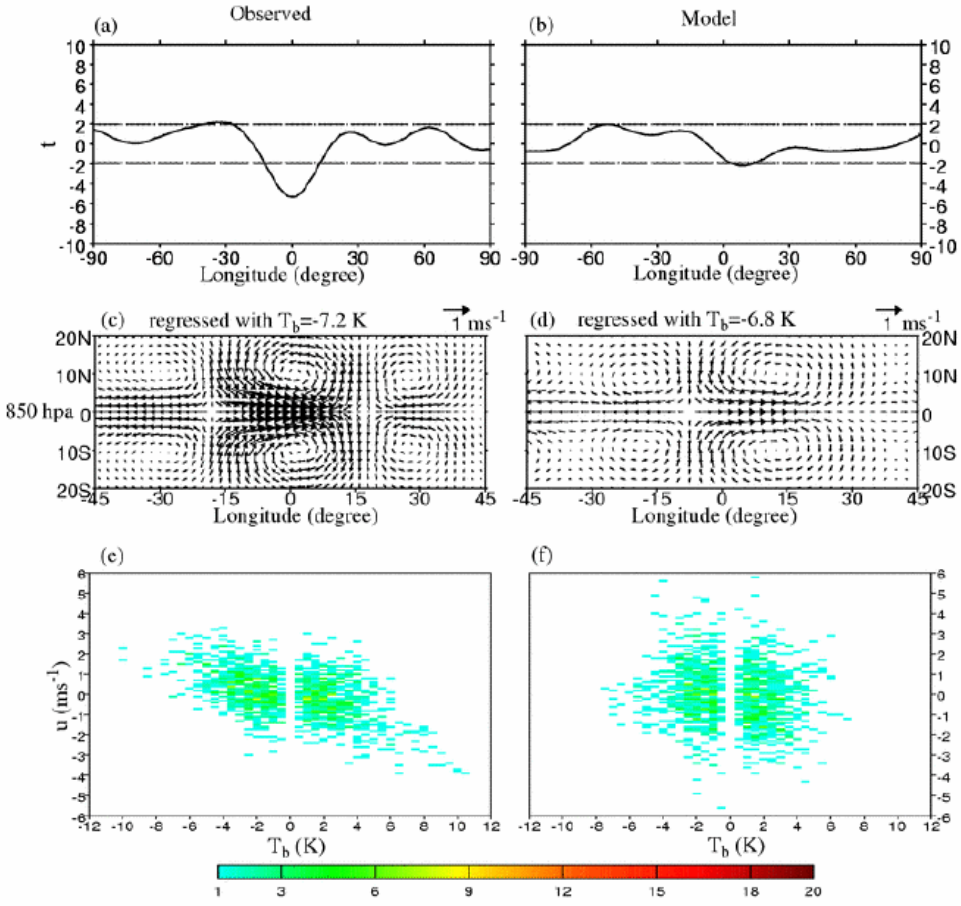

Figure 3.6. Relationship between equatorial convection and the equatorial zonal winds of the Rossby (n=1; R1) wave, showing evidence of wind-induced convection, for observations (left panels) and model (right panels). (a)-(b): As in Fig.3.3 but for the t-value of the relationship between the equatorial u of the westward moving R1 wave at 850hPa and equatorial convection (T_b at 5^{o}N-5^{o}S) in the eastern hemisphere. (c)-(d): Corresponding 850hPa R1 wave regressed against equatorial convective maxima. (e)-(f): Probability Distribution Function (PDF) of equatorial convection versus 850hPa zonal wind, corresponding to the case of 0^o longitude shift in (a) and (b).

A parallel diagnosis has been applied to the convective and dynamical fields from the HRES simulation, both for the model OLR and T_b derived from the OLR. For quantitative comparison we show the results for model converted T_b (right panels of Figs.3.3-3.6). Westward moving MRG and n=1 Rossby waves, coupled with off-equatorial convection, are quite well simulated, with significant correlations between the convective and dynamical fields, particularly for the MRG waves. The baroclinic structure of the MRG waves is successfully captured with a similar wavelength and upstream characteristics as seen in observations. However, convectively coupled Kelvin waves are poorly simulated by the model (Fig. 3.5, right panels), with only very local coupling between convection and winds, and with a wave-amplitude that is weaker than observed. This is consistent with the results shown in Figure 3.1 and the weaker variance in the model for the eastward moving equatorial convection noted earlier. In addition, the connection between anomalous equatorial zonal winds associated with the R1 wave and equatorial convection revealed in observations is not captured (Fig. 3.6, right panels). The missing link between the anomalous zonal winds and equatorial convective in the model may partly explain the weak variance of convection over most of the near equatorial region in the model.

In summary, these preliminary results have shown that although the model can simulate the dynamical aspects of equatorial waves, the coupling of these waves with convection, particularly in equatorial regions, is deficient. The potential role of wind-induced fluxes of moist entropy in triggering equatorial convection which can then modify and possibly amplify the waves appears not be present in the model. The reasons for this are unclear but merit investigation. It is notable that a major shortcoming of the model's simulation of the MJO is the lack of organization and variability in equatorial convection.

References:

Ohring, G. and A. Gruber, 1984: Satellite determination of the relationship between total longwave radiation flux and infrared window radiance. *J. Clim. Appl. Met.*, **23**, 416-425.

Wheeler, M. and G. N. Kiladis, 1999: Convectively-coupled equatorial waves: Analysis of clouds and temperature in the wavenumber-frequency domain. *J. Atmos. Sci.*, **56**, 374-399.

Yang, G. Y, B. Hoskins, and J. Slingo, 2003: Convectively coupled equatorial waves: A new methodology for identifying wave structures in observational data. *J. Atmos. Sci.*, in press.

4. Northern hemisphere storm tracks: Kevin Hodges and Brian Hoskins

A novel method for tracking features associated with middle latitude weather systems and producing diagnostic of the results has been applied to all the Reanalysis data sets and to some Hadley centre models. The technique gives a detailed dynamical picture of the middle latitude storm tracks. An initial comparison of the model performance with that observed formed the topic of a Reading PhD student (D. Anderson, CASE with the Hadley Centre). More recent work, the results of which are shown here, has been performed as a collaborative effort with the Hadley Centre.

Many fields have been considered and many diagnostics produced. The field used for the pictures shown here (850hPa relative vorticity) is a measure of the near surface cyclonic circulation that captures the essence of surface weather systems. The diagnostics are the average density of tracks passing through a region and the average intensity of the systems in those tracks (Figure 4.1).

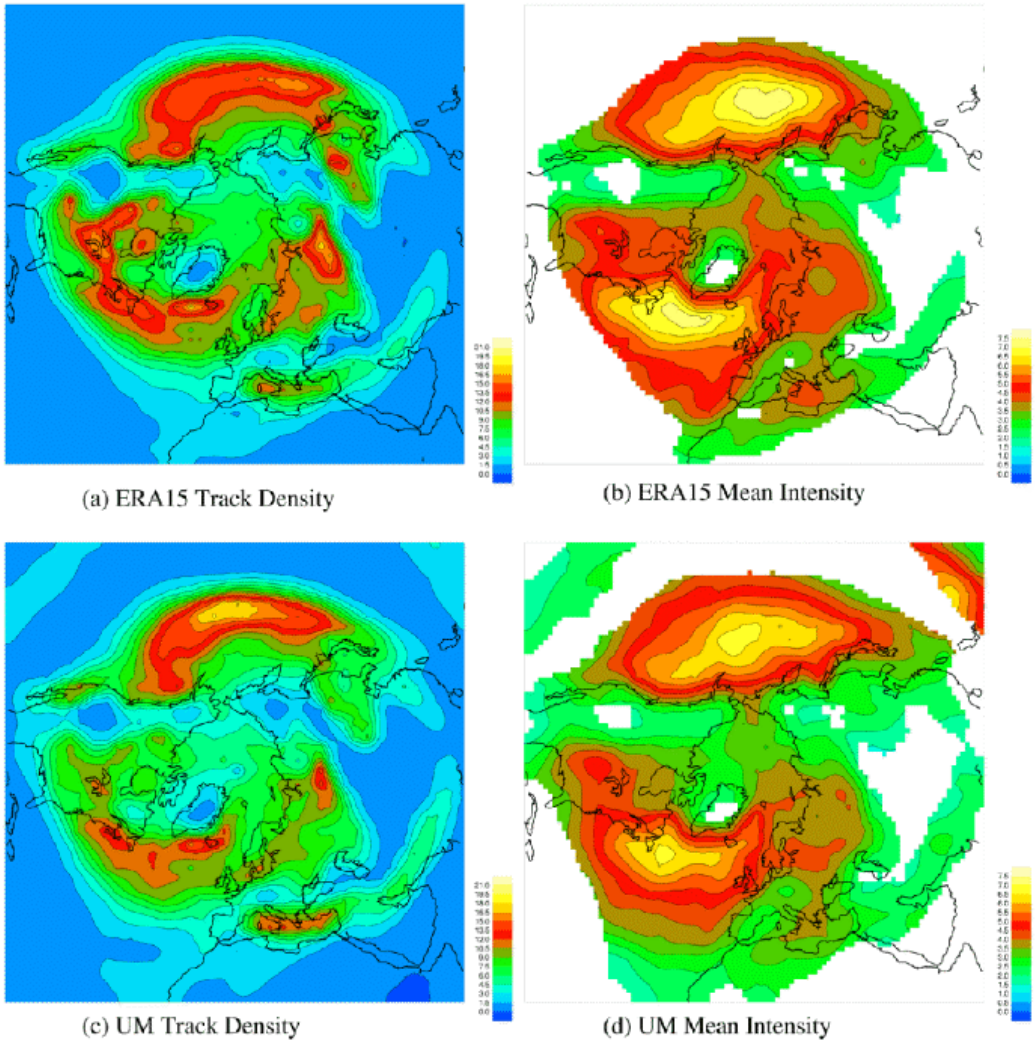

Figure 4.1. Northern Hemisphere winter storm track diagnostics derived from observed data (ERA-15), top panels, and from HadAM3 (N96L30), lower panels. (a) and (c) show the track densities, and (b) and (d) the mean intensities of systems.

The top panels in Fig. 4.1 give these diagnostics for the ERA-15 observational data for the northern hemisphere in winter. The storm tracks in the North Pacific and the North Atlantic both show up clearly as paths that many strong systems follow. There are also indications of northern Eurasian and Mediterranean storm tracks. The lower two panels, (c) and (d), in Fig 4.1 give the equivalent results from an AMIP II integration of HadAM3 at a resolution of N96L30. Its simulation of the northern hemisphere winter storm tracks is generally good. Looking in detail, the Pacific track density is too large and that in the Atlantic too weak. The lack of systems in the Atlantic storm track may be related to the lack of cyclonic activity upstream over North America, which may in turn be associated with the lack of systems originating along the eastern edge of the Rockies. In terms of the intensity, the weather systems are typically not quite as strong as they should be in HadAM3 for both storm tracks. The Eurasian and Mediterranean storm tracks are also weak.

The mean regions of genesis for extra-tropical weather systems have also been diagnosed (Figure 4.2). The results show the importance of the Rockies as the genesis region for weather systems, as well as the cyclogenesis in the lee of the Alps over the Mediterranean. HadAM3 shows considerable skill in capturing the main regions of cyclogenesis, although the results confirm the reduced levels along the eastern edge of the Rockies. The regions of secondary cyclogenesis over the oceans are also well captured by the model

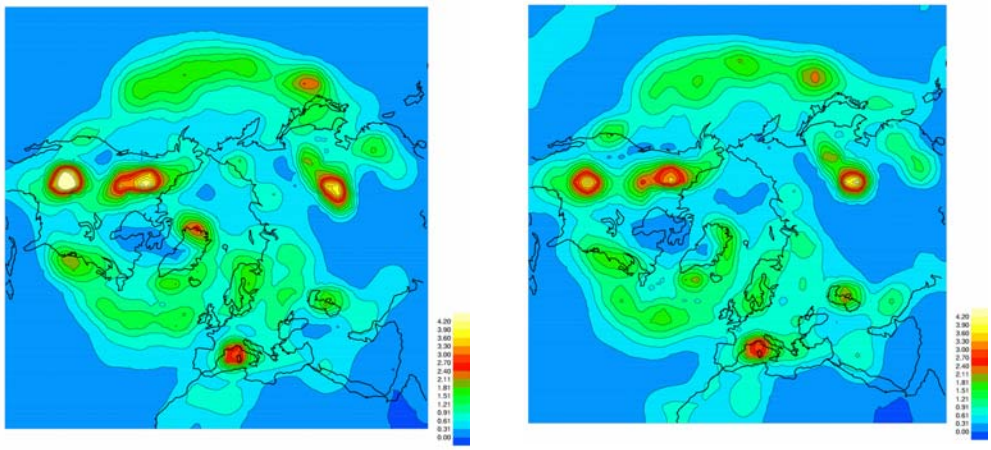

Figure 4.2: Mean genesis regions for cyclones in ERA-15 (left panel) and HadAM3 (right panel).

The results shown above raise the question of the sensitivity to resolution. Fig. 4.3 shows the differences in the track densities between runs of the model with various horizontal and vertical resolutions. The differences are not large but are still important, particularly in the Pacific. Panel (a) shows changes for increased horizontal resolution at high vertical resolution, (b) for increased vertical resolution at high horizontal resolution and (c) for changes in both. Detailed conclusions from this work have yet to be made. However there is an indication that horizontal and vertical resolution should be increased simultaneously.

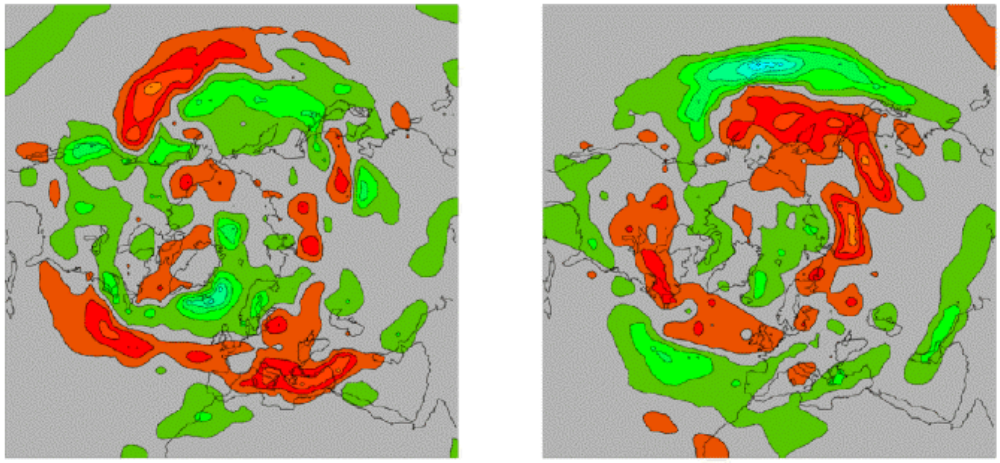

(a) N48L30 – N96L30

(b) N96L19 – N96L30

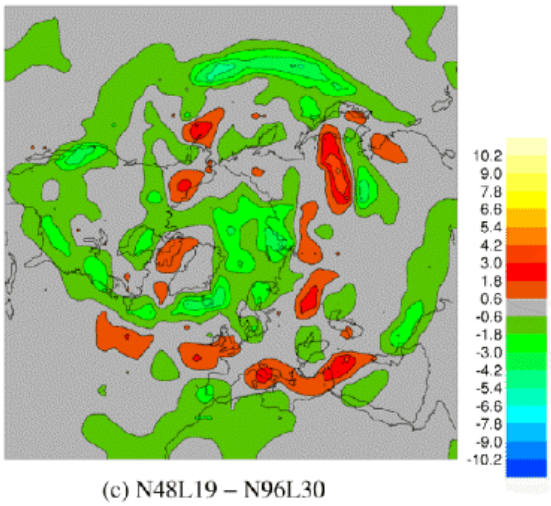

(c) N48L19 – N96L30

Figure 4.3. The difference in wintertime track densities between the indicated model resolutions. N48 to N96 indicates a doubling of the horizontal resolution and L19 to L30 indicates a change from 19 to 30 levels in the vertical. The model results shown in Figs.4.1 and 4.2 were with N96L30.

5. Impacts of increasing the vertical resolution of HadAM3 on the representation of tropical convection: Pete Inness and Julia Slingo

Experiments using HadAM3 with two different vertical resolutions show differences in the amount of variability in the tropical upper tropospheric zonal wind component associated with the Madden-Julian Oscillation (MJO; Inness et al. 2001). Figure 5.1 shows an index of this quantity from AMIP II integrations of HadAM3 with the different vertical resolutions, together with the same index calculated from ECMWF reanalysis winds. HadAM3 with the standard 19 vertical levels shows very little variability in this quantity whereas when the vertical resolution is doubled in the free troposphere giving 30 vertical levels, HadAM3 produces variability, which is of the same strength as observations. However, the eastward propagation of an enhanced convective region from the Indian Ocean into the west Pacific is not well represented in either simulation of this atmospheric GCM.

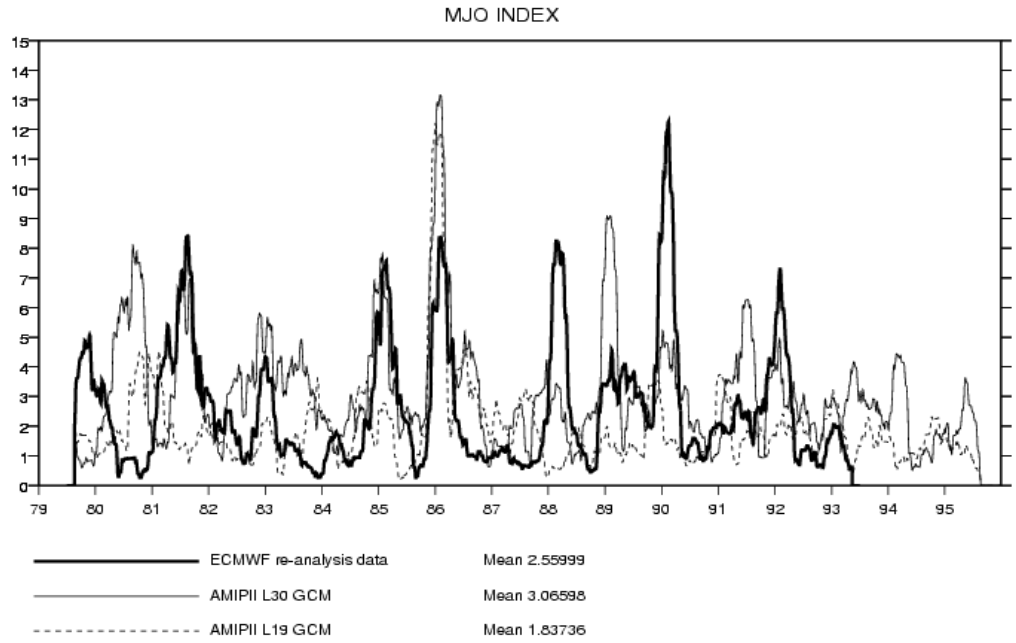

Figure 5.1. Index of MJO activity based on variance of 200 hPa zonal wind between 5^oN and 5^oS, from L19 and L30 versions of HADCM3, and ECMWF re-analysis data.

A water-covered or 'aqua-planet' version of HadAM3 has been used to investigate the behaviour of tropical convection when the vertical resolution is increased. The spectrum of tropical cloud types changes from a bimodal distribution with peaks representing shallow cumulus and deep cumulonimbus clouds to a trimodal distribution with a third peak in mid-troposphere near the melting level. Figure 5.2 shows the contribution to atmospheric moisture from the convection scheme in the form of a time-height section for a 3x3 grid-box region straddling the equator in both L19 and L30 versions of the model. In the L19 version, convection always acts to dry the troposphere indicating deep convection with detrainment just below the tropopause. In the L30 version there are significant periods when convection acts to moisten the mid-troposphere, and these periods are found to coincide with times when there is a strong mid-tropospheric inversion and cumulus congestus is the dominant cloud type.

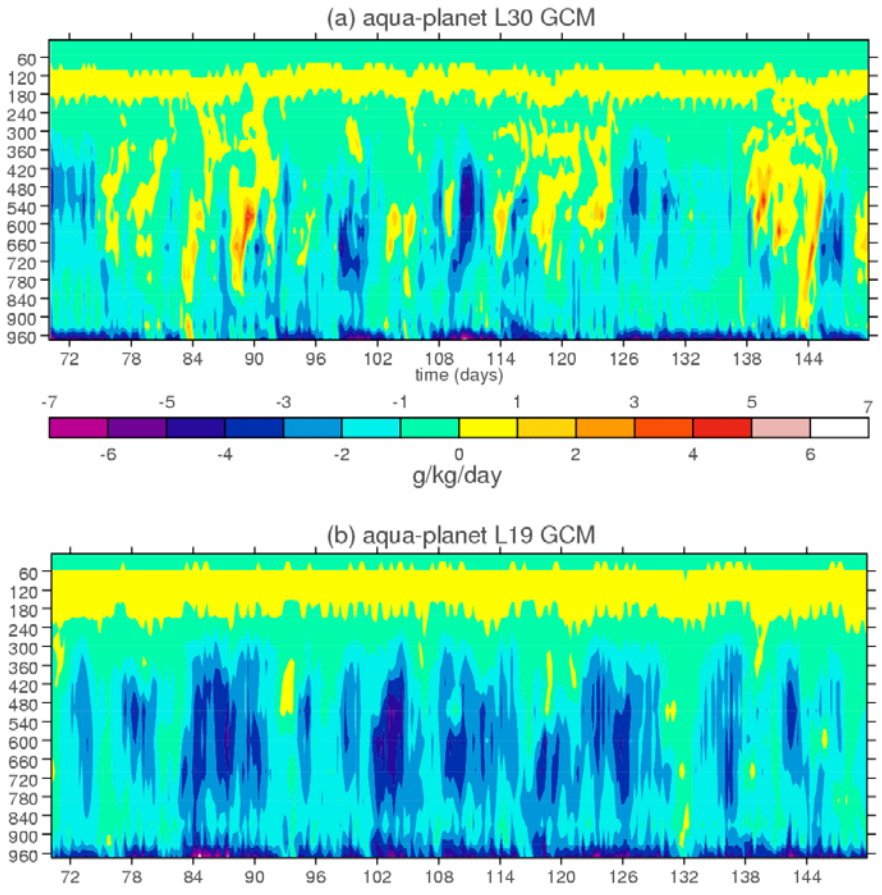

Figure 5.2. Time-height cross-sections of convective increment to specific humidity (g/kg/day) for a 90 day period from the aqua-planet integrations, averaged over a 3x3 grid-point box centred on the equator. (a) L30 aqua-planet. (b) L19 aqua-planet.

The appearance of these congestus clouds is shown to be partly due to improved resolution of the freezing level and the convective processes occurring at this level. In particular, the cooling due to melting of precipitation falling through the freezing level is distributed over a thinner layer resulting in a sharper inversion near the freezing level. However, due to the way in which convective detrainment is parametrized in the model, the vertical profile becomes rather noisy and this too contributes to the change in the nature of the convective clouds.

Observational studies have shown that, during the suppressed phase of the MJO, tropical convection is dominated by clouds that terminate around the stable layer at the 0^{o}C level (Johnson et al. 1999), and that these clouds provide a source of moisture to the mid-troposphere (Lin and Johnson 1996). Inness et al. (2001) argue that the development of a stable layer around the tropical melting level, which is frequently observed over the tropical oceans, acts to reinforce the transition from the enhanced convective phase to the suppressed phase of the MJO. Subsequently, the moistening of the mid-troposphere during the suppressed phase acts to reinforce the transition back to the active phase. This is consistent with the 'recharge-discharge' theory for the MJO proposed by Bladé and Hartmann (1993) in which the MJO timescale may be set by the time it takes for the moist static energy to build up following the decay of the previous convective event. It may be that the recharging of the moist static energy is achieved in part by the injection of moisture into the mid-troposphere by the

cumulus congestus clouds that dominate during the suppressed phase of the MJO.

The appearance of these congestus clouds has been postulated as the reason for the improvement in the simulation of the MJO in the 30-level version of the UM. This is shown to be partly due to improved resolution of the freezing level and of the convective processes occurring at this level. However, the results also suggest that convection and cloud microphysics schemes must be able to represent cumulus congestus clouds which, being neither shallow nor deep cumulus as well as often weakly precipitating, tend not to be explicitly represented in current schemes.

The results of Inness et al. (2001) have emphasized the importance of vertical resolution, in line with the recent study of Tompkins and Emanuel (2000), as well as the need to properly represent the tri-modal structure of tropical convection. The importance of the cumulus congestus stage of tropical convection is being stressed here as a potentially important ingredient for the MJO. This means that vertical resolution in the free troposphere must be adequate to resolve the formation of the freezing level inversion and the cooling associated with melting precipitation.

References:

Bladé I. And D. L. Hartmann, 1993: Tropical intraseasonal oscillations in a simple nonlinear model, *J. Atmos. Sci.* , **50**, 2922.

Inness, P.M, J.M. Slingo, S.J. Woolnough, R.B. Neale and V.D. Pope. 2001. Organization of tropical convection in a GCM with varying vertical resolution: Implications for the simulation of the Madden-Julian Oscillation. *Climate Dynamics*. **17**. 777-793.

Johnson, R., Ciesielski, P. E., and Hart, K. A. 1996. Tropical inversions near the 0^{o}C level. *J. Atmos. Sci.* **53**. 1838-1855.

Johnson, R. H., Rickenbach, T. M., Rutledge, S. A., Ciesielski, P. E., and Schubert, W. H. 1999. Trimodal characteristics of tropical convection. *J. Climate*. **12**. 2397-2418.

Lin, X. and R. H. Johnson, 1996: Heating, moistening and rainfall over the western Pacific warm pool during TOGA COARE. *J. Atmos. Sci..*, **53**, 3367-3383.

Tompkins, A. M. and K. A. Emanuel, 2000: The vertical resolution sensitivity of simulated cequilibrium tropical temperature and water vapour profiles. *Q. J. R. Meteorol. Soc.*, **126**, 1219- 1238.

6. Investigating the Madden-Julian Oscillation in HadCM3: Peter Inness and Julia Slingo

The simulation of the Madden-Julian Oscillation (MJO) has become something of a benchmark test for the performance of GCMs in the tropics over recent years. Many atmospheric GCMs have been shown to reproduce some aspects of the MJO, but have had problems representing its amplitude, propagation speed and seasonality. Recent observational and modelling studies (e.g. Flatau *et al*. 1997, Waliser *et al*. 1999) have suggested that the MJO is, at least to some extent, a coupled phenomenon. Thus with the complex interactions between convection and large scale dynamics, together with the interactions between the sea surface and boundary layer, the MJO provides a rigorous test for many aspects of a GCM formulation.

The ability of HadCM3 to represent various aspects of the MJO has been examined, and compared with the performance of the atmosphere-only component of the same model forced with slowly varying sea surface temperatures (Inness and Slingo 2003). One impact of coupling the GCM to an interactive ocean is to improve the eastward propagation of convection across the Indian Ocean. Figure 6.1 shows a composite of the MJO based on lag-correlation of the 20-100 day filtered convective precipitation in the equatorial strip with the 20-100 day filtered 200hPa velocity potential at 90^{o}E. Whilst the convection in HadAM3 shows no eastward propagation, the convective signal in HadCM3 shows eastward propagation across the Indian Ocean basin with a phase speed that is in good agreement with the observed MJO.

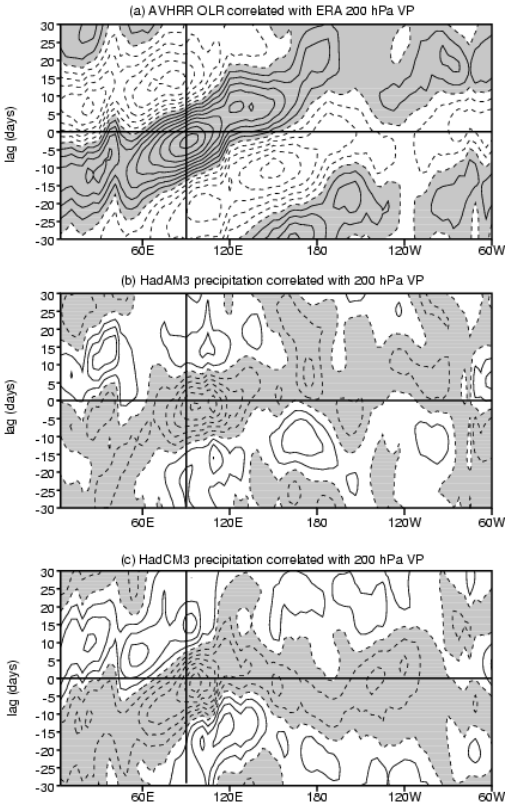

Figure 6.1: Lag correlation plots of OLR or convective precipitation averaged between 10^{o}N and 10^{o}S with 200 hPa velocity potential at 90^{o}E, also averaged between 10^{o}N and 10^{o}S. (a) NOAA AVHRR OLR correlated with ECMWF re-analysis velocity potential, (b) HadAM3 precipitation and velocity potential and (c) HadCM3 precipitation and velocity potential. Shading indicates negative correlations between precipitation and VP, and positive correlations between OLR and VP. Contour interval is 0.1. All data are 20-100 day band-pass filtered.

Detailed analysis of surface fluxes and SST variations associated with the MJO has been undertaken. The latent heat and short wave flux anomalies are in reasonable agreement with observations but the resulting SST variability is found to be slightly weaker than observed. This is thought to be due to the rather coarse resolution of the upper ocean in HadCM3 so that the intraseasonal flux variations are being distributed

through too deep a layer. There is no propagation of convection into the West Pacific in the coupled model. It is proposed that this deficiency is due to errors in the basic state of the coupled model, in particular the lack of low-level westerly winds over West Pacific.

The impact of these systematic errors has been investigated (Inness et al. 2003). An integration of HadCM3 with limited flux-adjustment in the equatorial Pacific has been performed which has reduced basic state errors in the West Pacific. Figure 6.2 shows the 850 hPa zonal wind climatology from the standard and flux-adjusted versions of HadCM3 for the October through April period. Note the extension of westerly winds into the West Pacific in the flux-adjusted version.

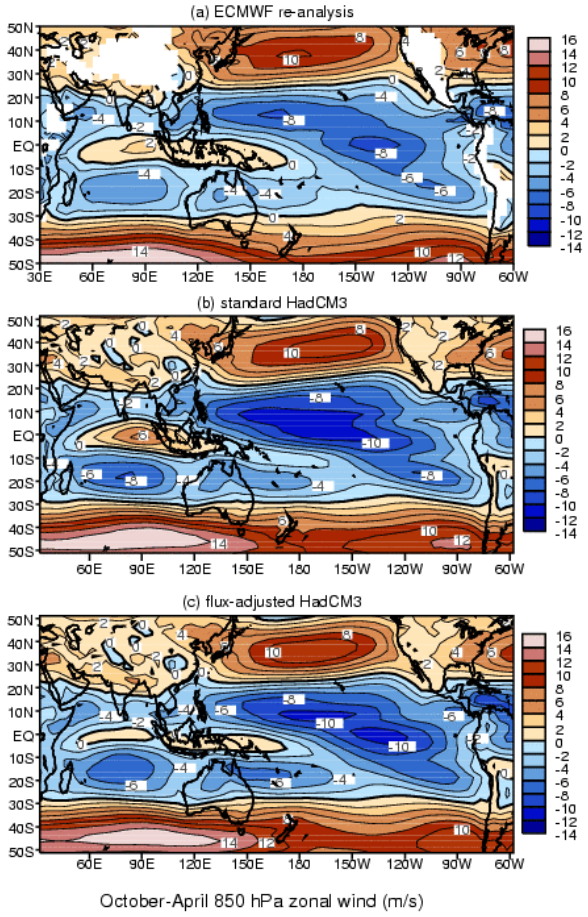

Figure 6.2: October-April zonal wind climatologies from (a) ECMWF reanalysis (b) HadCM3 and (c) HadCM3 with limited flux adjustment. Contour interval is 2ms^{-1}.

In the flux-adjusted version of HadCM3 the MJO does propagate into the West Pacific as shown in Figure 6.3, although the convective signal is weaker and less robust in the Indian Ocean basin. The simulation of the MJO by a coupled model with the same atmospheric component but a different ocean GCM (the HadOPA configuration) has also been analysed. This coupled GCM has similar systematic errors in low level zonal wind and precipitation to HadCM3, but with warmer SSTs. Results from this experiment, together with the other available evidence, suggest that it is the errors in the low-level zonal wind component in the West Pacific which prevent the MJO from propagating into this region in HadCM3 rather than the errors in absolute values of SST.

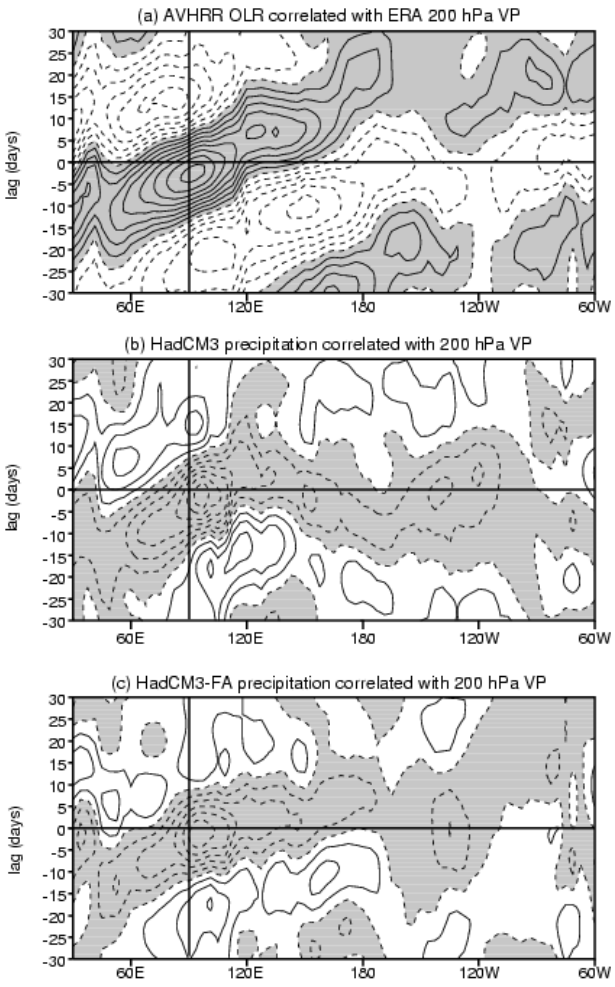

Figure 6.3: Lag correlation plots of OLR or convective precipitation averaged between 10°N and 10°S with 200 hPa velocity potential at 90°E, also averaged between 10°N and 10°S. (a) NOAA AVHRR OLR correlated with ECMWF re-analysis velocity potential, (b) HadCM3 precipitation and velocity potential and (c) HadCM3 with flux adjustment precipitation and velocity potential. Shading indicates negative correlations between precipitation and VP, and positive correlations between OLR and VP. Contour interval is 0.1. All data are 20-100 day band-pass filtered.

References:

Flatau, M., P. J. Flatau, P. Phoebus and P. P. Niiler. 1997. The feedback between equatorial convection and radiative and evaporative processes: The implications for intraseasonal oscillations. *Journal of Atmospheric Science*. **54**. 2373-2386.

Inness, P. M. and J.M. Slingo. 2003. Simulation of the Madden-Julian Oscillation in a coupled general circulation model I: Comparison with observations and an atmosphere-only GCM. *Journal of Climate*. **16**. 345-364.

Inness, P.M., J.M.Slingo, E. Guilyardi and J. Cole. 2003. Simulation of the Madden-Julian Oscillation in a coupled general circulation model II: The role of the basic state. *Journal of Climate*. **16**. 365-382.

Waliser, D. E., K. M. Lau and J-H. Kim. 1999. The influence of coupled sea surface temperatures on the Madden-Julian oscillation: a model perturbation experiment. . *Journal of Atmospheric Science*. **56**. 333-358.

7. The Sensitivity of North Pacific/North American El Niño Teleconnections to the Modelling of Tropical Pacific Precipitation: Hilary Spencer

In order to achieve accurate seasonal forecasts, the teleconnections of El Niño and La Niña must be modelled accurately. It has been shown that the teleconnections across the North Pacific and North America are very sensitive to the simulation of the tropical Pacific precipitation anomalies (Spencer and Slingo 2003). A six-member ensemble of HadAM3, at climate resolution (N48L19) with observed sea surface temperatures (SSTs) for 1948 to 1998, has been used to construct composite anomalies for years with a strong El Nino that peaks in northern winter (DJF). The ensemble mean composite anomalies are compared with those from the NCEP reanalysis data for the same years (Figure 7.1).

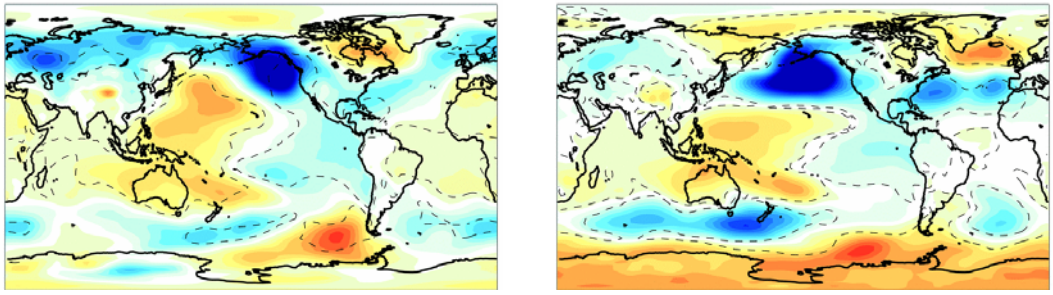

Figure 7.1: Composite PMSL anomalies for DJF at the peak of El Nino from NCEP Reanalyses (left panel) and HadAM3 (right panel). The anomalies enclosed by dashed lines are significant at the 95% level.

The results have shown that while the model captures successfully the surface pressure anomalies in the tropics, basically the Southern Oscillation, its simulation of the extratropical response to El Nino is less successful. Instead of the eastwards displacement of the Aleutian Low, HadAM3 shows an in situ deepening. This is associated with the lack of development of the anomalous ridge over the north and west Pacific. The displacement of the response over the north Pacific leads to downstream errors over North America. HadAM3 also shows a significant projection of ENSO on to the North Atlantic pressure pattern, characteristic of the NAO, which is not seen in the reanalyses. Other sensitivity experiments with HadAM3 (not shown here) have also shown a marked tendency for ENSO to excite a NAO-type pattern over the N. Atlantic.

Since the extratropical response to tropical SST anomalies is forced by the upper level outflow from tropical convection, the source of the errors in the PMSL patterns noted above has been sought in the tropical precipitation anomalies. Figure 7.2 shows the composite total precipitation fields for the same El Nino events from the NCEP reanalyses and HadAM3[1]. The results show that although HadAM3 simulates enhanced precipitation in the central tropical Pacific during El Nino, the absolute maximum in heating remains in the West Pacific. This is in contrast to the expected transition eastwards of the maximum precipitation seen in the NCEP Reanalyses. This means that the divergent outflow from the convection over the tropical Pacific, which provides the Rossby wave source for the extratropical teleconnections, is displaced

[1] Although the shortcomings of the precipitation in the NCEP Reanalyses are acknowledged, a comparison between NCEP and the CMAP climatology for El Nino events after 1979 has shown that the patterns are realistic although the amplitude may be underestimated.

westwards in HadAM3. It is argued by Spencer and Slingo (2003) that this displacement is responsible for the errors in the extra-tropical response to ENSO noted in Figure 7.1.

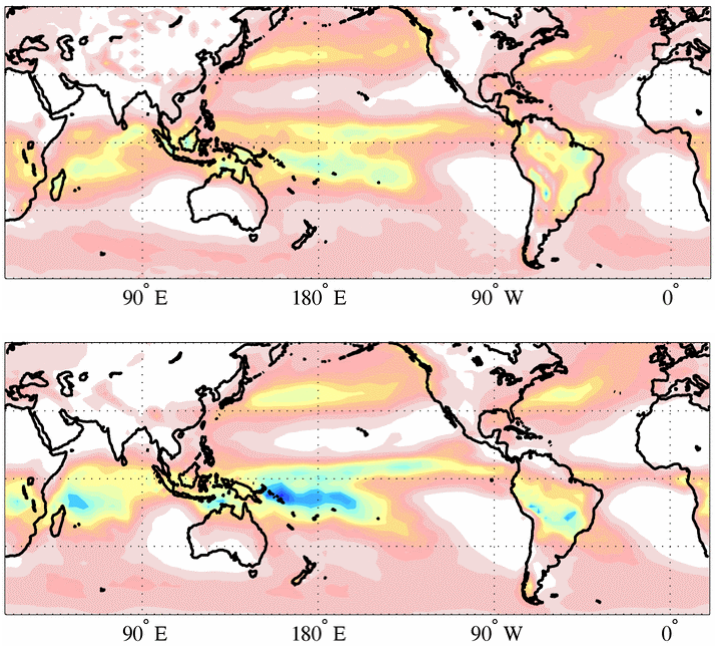

Figure 7.2: Composite total precipitation fields for DJF at the peak of El Nino from NCEP Reanalyses (left panel) and HadAM3 (right panel).

The errors in HadAM3's precipitation field over the tropical Pacific have been linked to the sensitivity of the model to SST. Figure 7.3 shows the probability distribution functions (PDF) of the SST and precipitation over the tropical Pacific for DJF based on monthly mean data from the NCEP Reanalyses and HadAM3.

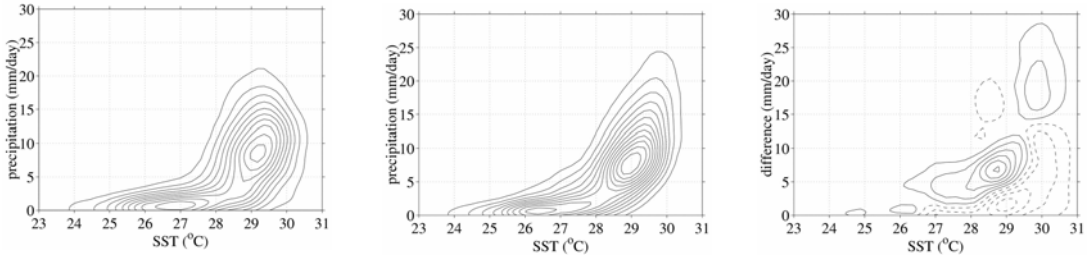

Figure 7.3: Probability distribution functions (PDF) of the SST and precipitation over the tropical Pacific for DJF based on monthly mean data from the NCEP Reanalyses (left panel) and HadAM3 (middle panel). Difference between the PDFs from NCEP and HadAM3 is shown in the right hand panel.

The results show the tendency for HadAM3 to overestimate precipitation over the warmest SSTs. One possible explanation for this is that the lack of coupling in an atmosphere-only model, prevents the expected negative feedback between convection and very warm SST that acts to regulate SSTs in the real world. Figure 7.3 also shows that the PDF from HadAM3 is too tight, following too closely the exponential relationship implied by the Clausius-Clapeyron equation for saturated vapour

pressure. The difference in the PDFs suggests that HadAM3 is unable to capture the low precipitation amounts observed over warm SSTs. One possible explanation for this is the lack of an MJO in the model, which would produce more variability in the precipitation over the tropical Pacific. The PDFs shown in Figure 7.3 are, potentially, a useful diagnostic for exploring the relationship between SST and convection, and could probably be usefully extended to cover higher frequency data from both atmosphere-only and coupled versions of the model.

The sensitivity of the performance of HadAM3 to vertical resolution has already been noted in Section 5 for the MJO. A notable improvement in the ENSO teleconnections in the L30 version of HadAM3 has also been found (Figure 7.4). The eastwards displacement of the Aleutian Low is now successfully captured. This has been linked to an improved simulation of the precipitation field over the tropical Pacific, confirming the association between the location of the tropical precipitation maximum and the errors in the extratropical teleconnections. Furthermore, the shape of the PDF of SST with precipitation (not shown) from the L30 version of the model shows a broader and more realistic distribution. Again this is consistent with the improved simulation of the MJO in the L30 model (see Section 5).

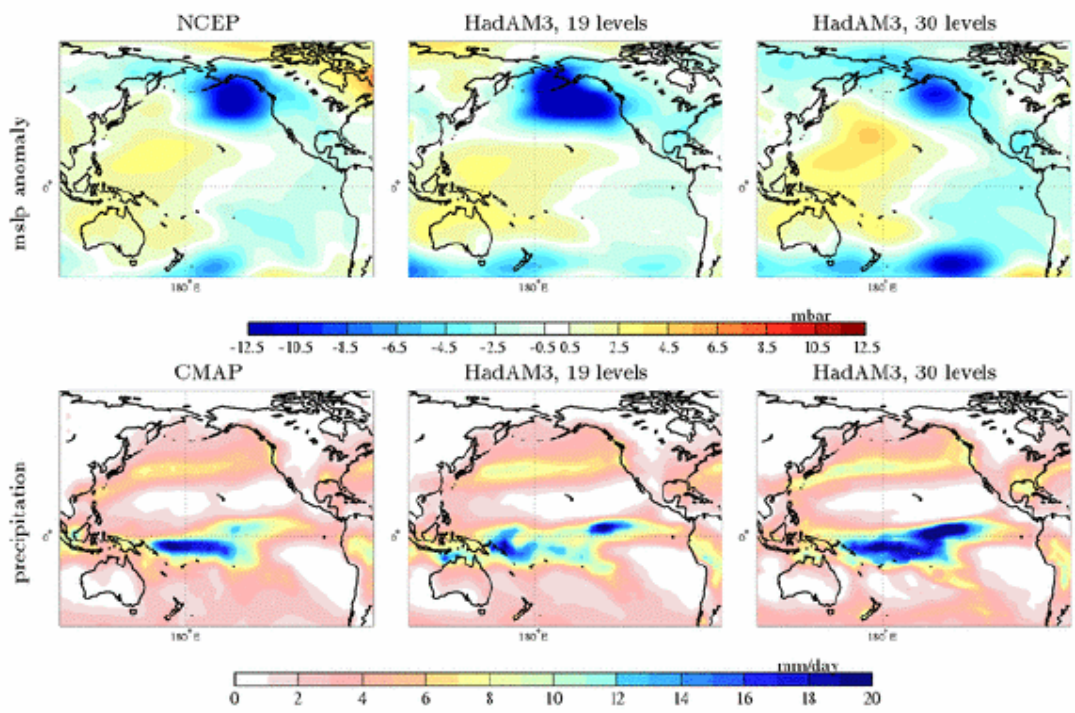

Figure 7.4: Comparison of the PMSL anomalies and total precipitation for DJF of 1982/83 from 'observations' and from the L19 and L30 versions of the HadAM3.

Reference:

Spencer, H. and J. M. Slingo, 2003: The simulation of peak and delayed ENSO teleconnections. *J. Clim.*, in press.

8. The climate of the Maritime Continent: Rich Neale, Julia Slingo

The Maritime Continent, with its complex system of islands and shallow seas, presents a major challenge to models, which tend to systematically underestimate the precipitation in this region (Fig. 8.1; Neale and Slingo 2003). Neale and Slingo (2003) argued the deficient rainfall over the Maritime Continent could be a driver for other systematic errors, such as the excess precipitation over the western Indian Ocean.

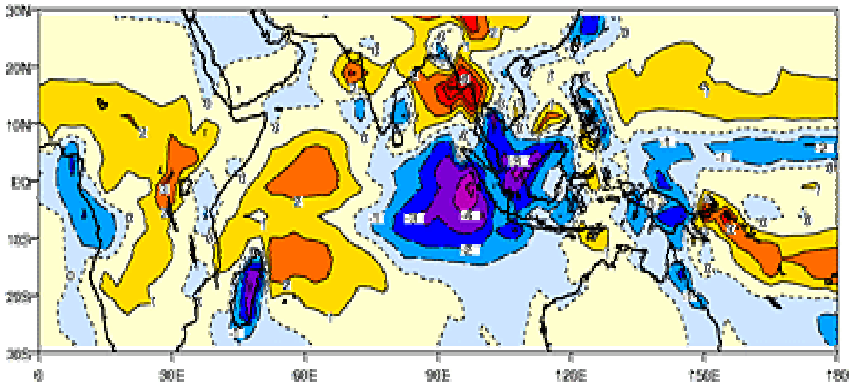

Figure 8.1: Annual mean precipitation errors (mm/day) from the AMIP II simulation with N48L19 HadAM3. The errors have been computed against the CMAP climatology.

To demonstrate the sensitivity of global systematic model errors to the heating in this region, Neale and Slingo (2002) performed two experiments, one with the existing distribution of islands and a second where the island grid-points are replaced by sea grid-points with SST interpolated from existing adjacent grid-point values. Both experiments were run for 17 years using observed SSTs for 1979-95. In the absence of the islands of the Maritime Continent, the local precipitation increases, reducing the existing dry bias and bringing the model closer to observations (Fig. 8.2).

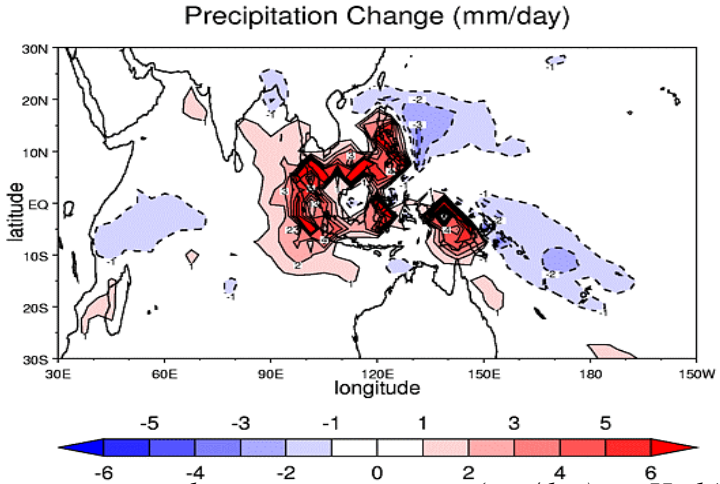

Figure 8.2: Change in annual mean precipitation (mm/day) in HadAM3 when the islands of the Maritime Continent are removed.

In response to this improved heating distribution, precipitation decreases over the West Indian Ocean and South Pacific Convergence Zone (SPCZ), reducing the systematic wet bias in these regions (see Figure 8.1). This supports the hypothesis that tropical systematic errors are often related through vertical (Walker) circulations.

The extra-tropical response to changes in the tropical heat source is also well demonstrated by these experiments. The enhanced heating and hence divergent outflow over the Maritime Continent generates Rossby waves which have a significant impact on northern hemisphere winter surface temperatures across much of North America and the North East Eurasian region (Fig. 8.3). These changes in mid-latitude circulation and surface temperature are such as to substantially reduce model systematic error in these regions. To check the robustness of these results, a second AMIP II integration was performed and very similar extratropical responses found. These results reinforce the critical role played by the Maritime Continent in the global circulation, and emphasize the importance of considering the global context of model systematic error in which biases in the tropics may be a key factor.

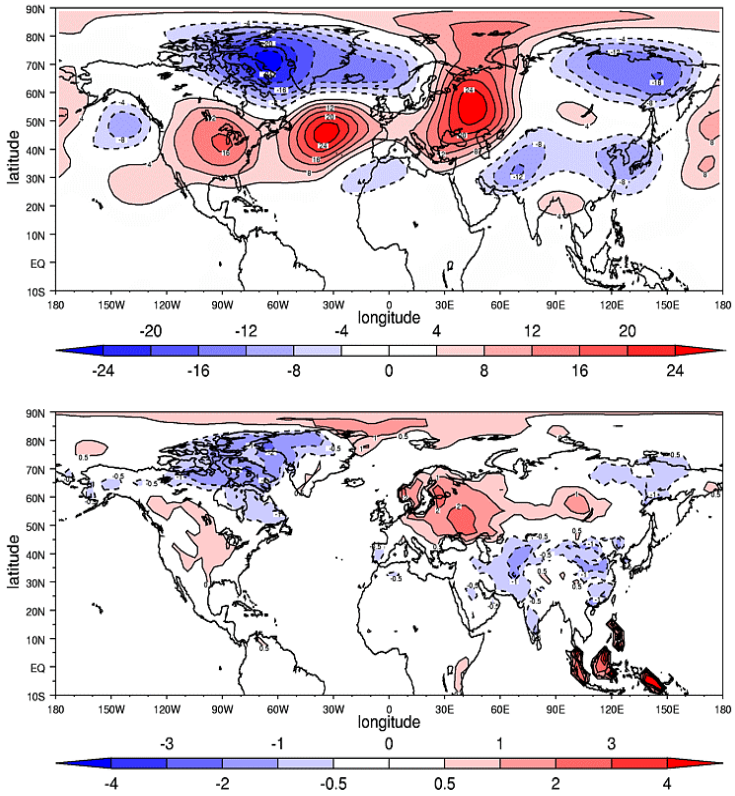

Figure 8.3: Seasonal mean changes in the 500hPa geopotential height (m) and surface temperature (K) for DJF, showing the global impacts of an improved heat source over the Maritime Continent.

It could be argued that this system of islands is poorly resolved at the coarse climate resolution of the model, but Neale and Slingo (2002) further showed that even with a three-fold increase in horizontal resolution there is no improvement in the dry bias of the model; if anything it seems to get slightly worse (Fig. 8.4). Additionally, the anomalously wet regions in the SPCZ and north and west of the Philippines are worse in the experiments with the highest resolution. The results in Figure 8.4 demonstrate very clearly the persistence of model errors and reinforce the notion that increasing resolution is not necessarily a panacea for model error, with the suggestion that deficiencies in the representation of the physical system are primarily responsible.

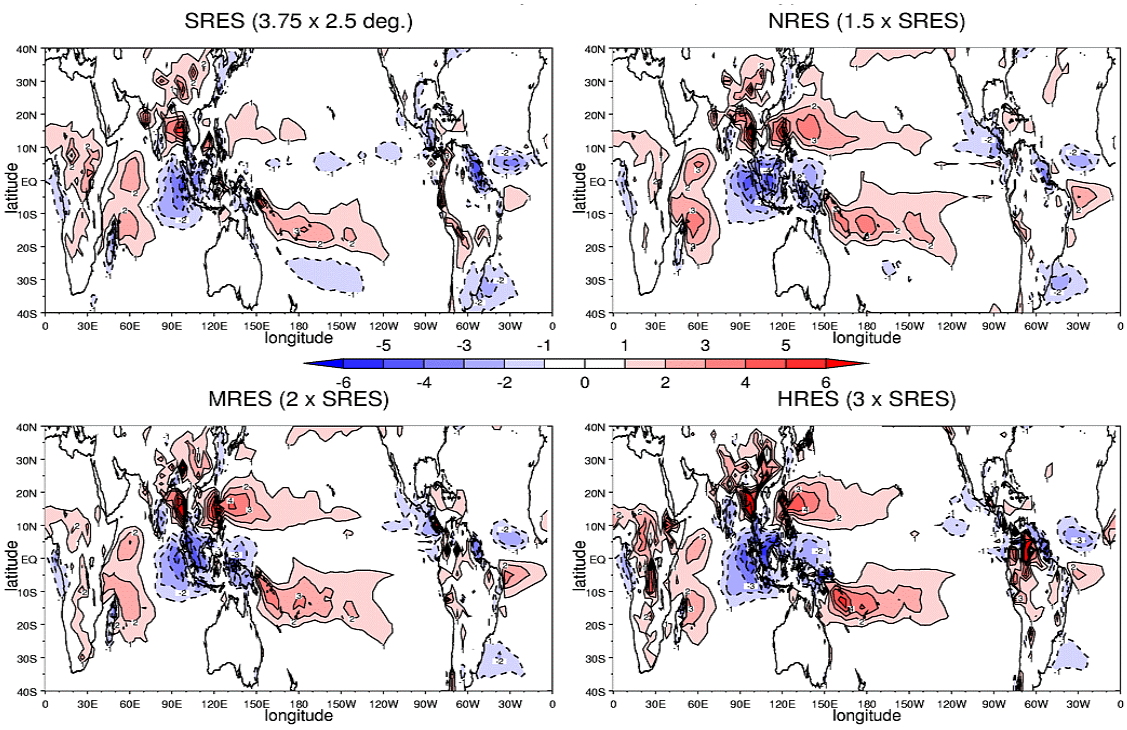

Figure 8.4: Annual mean precipitation errors (mm/day) from AMIP II integrations of HadAM3 at a range of horizontal resolutions.

The results summarized above clearly show that the Maritime Continent heat source is a key component of the global climate, and that improvements in its simulation may have significant impacts on remote systematic errors. The fact that many models show similar problems over the Maritime Continent suggests that they all lack some key ingredient. Neale and Slingo (2003) hypothesized that the diurnal cycle over the islands and the complex circulation patterns generated by land-sea contrasts may be crucial for the energy and hydrological cycles of the Maritime Continent and for determining the mean climate.

Evidence for the existence of these land-sea breezes has been provided by the detailed study of the diurnal cycle described in Section 2 and in Yang and Slingo (2001). The schematic presented in Figure 8.5 shows that a land/sea breeze has two major impacts – (i) convergence along the land/sea breeze front provides additional convective mass flux, and (ii) the winds associated with land/sea breezes enhance surface fluxes leading to increased moisture supply. A parametrization of these effects is under development using a mesoscale model to assess the magnitudes of the various components.

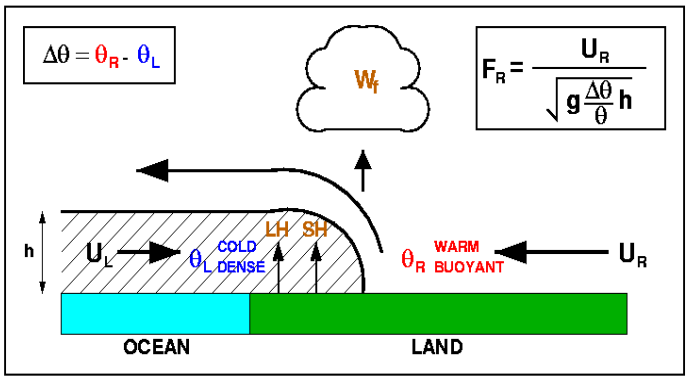

Figure 8.5: Schematic of a sea breeze showing the principal components that need to be included in the parametrization of its sub-grid scale effects.

References:

Neale, R. B. and J. M. Slingo, 2003: The Maritime Continent and its role in the global climate system: A GCM study. *J. Clim.,* **16**, 834-848.

Yang, G-Y. and J. M. Slingo, 2001: The diurnal cycle in the tropics. *Mon. Weath. Rev.*, **129**, 784-801.

9. El Nino in HadCM3, HadOPA, and results from PRISM modular modelling: Eric Guilyardi, Rich Neale, Julia Slingo

9.1: Tropics wide teleconnections in HadCM3

HadCM3 is known to have an exaggerated tropics-wide response to El Nino, which has a strong projection on to the global mean temperature. This tropics wide behaviour is well demonstrated in Figure 9.1, which shows the lag correlations between the Nino3 index and tropical SSTs from the model (upper three panels) and from the GISST dataset (lower three panels). The lagged response to El Nino in the tropical Indian and Atlantic Oceans is evident in the increased correlations with a lag of 6 months.

Although the response of the Indian Ocean to El Nino is well captured by HadCM3, Figure 9.1 shows some significant errors in the tropical Atlantic. The response is too close to the equator and the correlations are too high at lags of both zero and 6 months. Also evident in Figure 9.1 are various errors in the structure of El Nino in HadCM3, such as the equatorial confinement of the SST anomalies, the excessive westwards extension of the anomalies, and the regular, 3-year periodicity of El Nino (see appearance of negative correlations at a lag of 18 months). All of these factors contribute to the model's exaggerated tropics-wide and global mean temperature response to El Nino.

It is well known that the tropics-wide ocean response to El Nino is driven by the direct atmospheric response to an El Nino event, the so-called 'atmospheric bridge'. SST anomalies in the remote ocean basins can be forced through changes in surface latent heat flux due to anomalous surface winds, as well as through changes in the solar heating associated with perturbations to the Walker Circulation. Since the latent heat flux depends on the magnitude of the wind, it is clear that changes in the latent heat flux will be dependent on the basic state near-surface winds. A study of the remote response to El Nino in the tropical Atlantic has shown that the errors highlighted in Figure 9.1 are largely due to interactions with an erroneous basic state in HadCM3. In observations (Fig. 9.1, lower panels), the largest correlations and SST signal are north of South America whereas in HadCM3 the strongest correlations are found just north of the equator across the whole of the tropical Atlantic. Analysis of the seasonal cycle shows that at the peak time for the El Nino signal to affect the tropical Atlantic - usually February-March following the peak in east Pacific SST in December - the basic state winds, north of the equator, are weak westerlies rather than the observed climatological easterlies. This proves to be crucial, since any anomalous easterlies as a result of changes in the Walker Circulation brought about by El Nino, now *reduce*, instead of enhance, the latent heat flux from the ocean surface. This reduced heat loss acts in unison with increased surface insolation from suppressed convection, and combined with a shallower mixed layer, leads to the strong tropical Atlantic SST response seen in the model.

The key error in the model is therefore the basic state winds over the tropical Atlantic. Further analysis has traced these erroneous surface westerlies to the lack of marine stratocumulus over the south Atlantic, off the African coast - a generic problem in the UM. The resulting increased surface insolation eventually leads to a local positive SST bias in the Gulf of Guinea and an erroneous early African monsoon, with the establishment of westerly flow from the tropical Atlantic into Africa. So the consequences of the poorly modelled stratocumulus extend to the seasonal cycle of the tropical Atlantic and to the coupled response to a Pacific El Nino event.

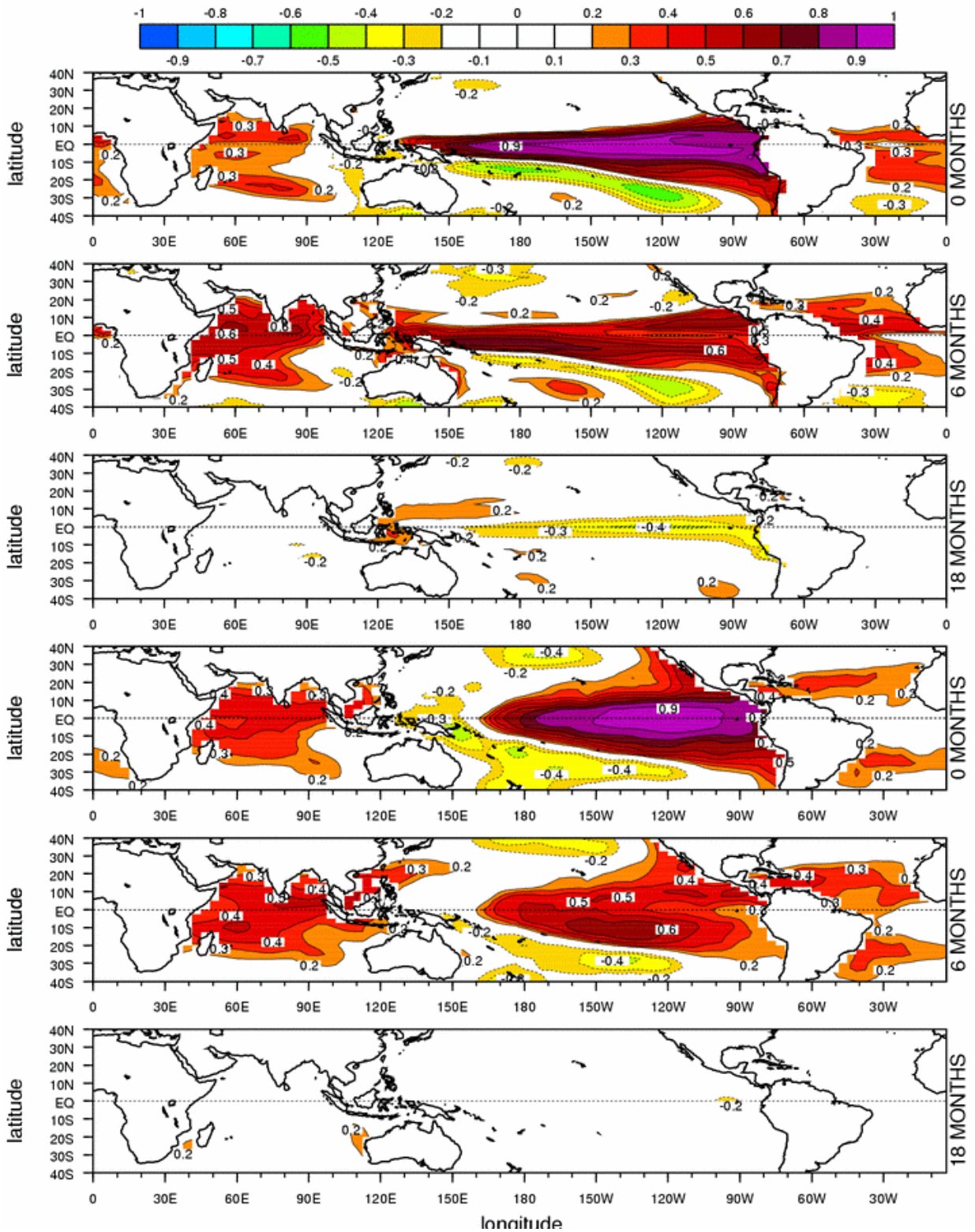

Figure 9.1: Correlations at lags of zero, 6 and 18 months between the Nino3 and tropics-wide SSTs from 100 years of coupled simulation with HadCM3 (three upper panels) and from the GISST3 dataset (three lower panels).

9.2 Role of atmosphere in determining El Nino behaviour in Hadley Centre models.

A new approach to investigating the respective roles of the ocean and atmosphere in setting the amplitude and frequency of El Nino in coupled models has been pioneered in CGAM (Guilyardi et al. 2003). A systematic modular approach has been developed where one component model (ocean or atmosphere) is coupled to a number of models of the other component (atmosphere or ocean). This has been applied to a family of Hadley Centre models in which HadAM3 is coupled to ocean models of differing formulation and resolution (HadOM3 i.e. HadCM3; the French ocean model, OPA i.e. HadOPA; eddy permitting version of HadOM3 i.e.HadCEM).

Initial analysis has focused on the amplitude and periodicity of El Nino (Figure 9.2). This shows several important aspects of El Nino in the model. Whereas the observations show that El Nino occurs over a broad range of frequencies between 3 and 7 years, none of the Hadley Centre models capture the low frequency mode of the observed phenomenon. Instead all show a concentration of power at a single, preferred frequency of 3 years, also noted in Figure 9.1. However, the most striking result in Figure 9.2 is the preference for a three-year El Nino cycle, *regardless* of which ocean component or ocean resolution is used. This result, demonstrating that the atmosphere apparently controls the periodicity of El Nino, is new and raises some important issues that are discussed in detail in Guilyardi et al. (2003).

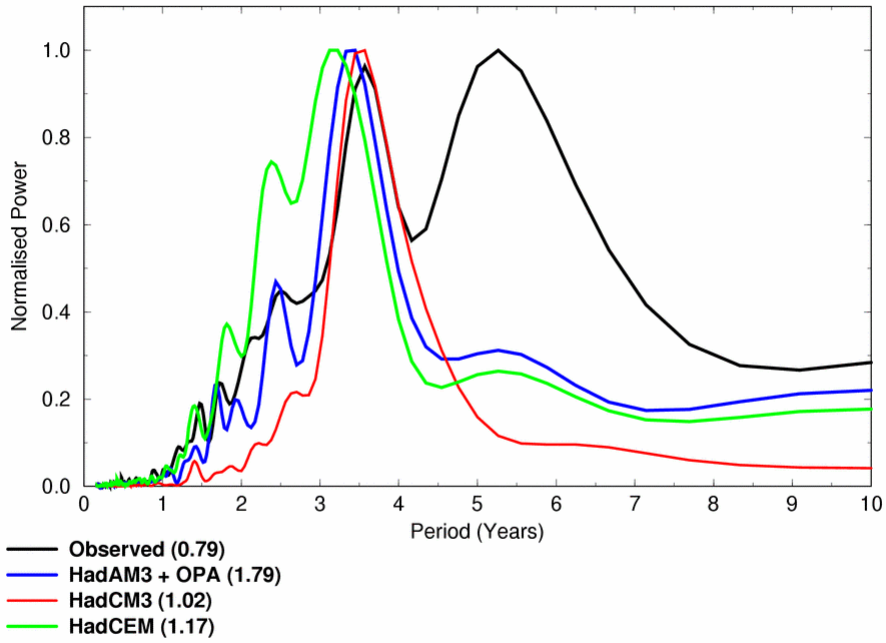

Figure 9.2: The normalized power spectra of the monthly SST in Niño3 region, (5^0S to 5^0N, 150^0W to 90^0W). The reference observations are obtained from 100 years (1900-1999) of the HadISST1.1 dataset. The normalization has been done with respect to the peak power in the spectrum. As a measure of the amplitude of El Nino, the standard deviation of the Niño3 SST time series is shown in brackets.

Figure 9.2 also shows that the amplitude of El Nino is too high in the model, particularly when HadAM3 is coupled to OPA. Again evidence from a parallel analysis of versions of the ECHAM coupled model points to the atmosphere as providing the primary control on the strength of El Nino, although ocean model

characteristics can modify it slightly. For example, sensitivity experiments with HadOPA, in which the ocean vertical mixing scheme was changed to that in HadOM3, reduced the El Nino amplitude slightly to 1.4^0C, but left the dominant frequency unchanged. Also, increasing the viscosity in OPA to that of HadOM3 was shown to have little impact on El Nino characteristics.

Guilyardi et al. (2003) argue that the coupling strength between the atmosphere and ocean, known to be a key parameter for El Nino frequency in simple coupled models, may be a factor here also. Physically, the coupling strength measures how strongly the atmospheric winds will respond to SST anomalies, and might be expected to depend on the boundary layer and convective parametrizations. Preliminary results from an integration of HadOPA with CAPE closure on the convection scheme suggest, however, limited sensitivity.

It is notable that all the coupled versions of the UM used in this study have stronger than observed trades winds. According to idealised modelling results (e.g Fedorov and Philander 2000), these may reduce the model's sensitivity to SST changes and shorten the periodicity of El Nino. Secondly, several studies have suggested that the meridional extent of the atmospheric response to tropical SST anomalies can influence the frequency of El Nino (e.g. Kirtman 1997), with a broader meridional response of the wind generating forced Rossby waves further off-equator. These waves therefore provide a slower negative feedback to the El Nino turn-about in the West Pacific, lengthening the period between two El Nino events. A notable problem with the Hadley Centre coupled models is the equatorial confinement of the SST signal associated with El Nino, as seen in Figure 9.1, suggesting that basic state errors may be a factor in setting the characteristics of El Nino in the model.

There is increasing evidence that intraseasonal atmospheric variability, especially the Madden Julian Oscillation (MJO), may play a crucial role in the initiation and amplification of El Nino (e.g. Lengaigne et al. 2003), and may introduce a stochastic forcing into the coupled system. Although there is some evidence that the MJO is better simulated in HadCM3 (e.g. Inness and Slingo 2003), basic state errors in the tropical Pacific prevent its propagation eastwards and limit westerly wind activity over the equatorial West Pacific (Inness et al. 2003). So it is likely that the combination of weak intraseasonal activity and basic state errors may limit the stochastic forcing of El Nino by the atmosphere and contribute to its regularity in Hadley Centre coupled models.

References:

Fedorov, A. V. and S. G. Philander, 2000: Is El Nino changing? *Science*, **208**, 1997-2002.

Guilyard, E., and others, 2003: Does the atmosphere set the timescale for El Nino? Answers from a modular approach to coupled ocean-atmosphere modelling. Submitted to *Science.*

Inness, P. M. and J.M. Slingo. 2003. Simulation of the Madden-Julian Oscillation in a coupled general circulation model I: Comparison with observations and an atmosphere-only GCM. *Journal of Climate*. **16**. 345-364.

Inness, P.M., J.M.Slingo, E. Guilyardi and J. Cole. 2003. Simulation of the Madden-Julian Oscillation in a coupled general circulation model II: The role of the basic state. *Journal of Climate*. **16**. 365-382.

Kirtman, B. P., 1997: Oceanic Rossby wave dynamics and the ENSO period in a coupled model. *J. Climate*, **10**, 1690-1704.

Lengaigne, M., J-P. Boulanger, C. Menkes, G. Madec, P. Delecluse, E. Guilyardi and J. Slingo, 2003: March 1997 Westerly Wind Event and the onset of the 1997/98 El Nino: Understanding the role of the atmospheric response. *J. Clim* (in press)

10. Seasonally varying vegetation in MOSES-2 and biosphere-atmosphere interactions: Dave Lawrence

A primary focus of our research has been to assess the impact of an imposed vegetation annual cycle on climate and hydrology in HADAM3-MOSES2 (Lawrence and Slingo 2003a,b).

A vegetation annual cycle for each plant functional type (PFT) in each gridbox has been derived from satellite estimates of Leaf Area Index (LAI) obtained from the nine-year ISLSCP II dataset by using the ISLSCP II LAI climatology in conjunction with a 1^o by 1^o version of the IGBP landcover dataset. For each PFT in each model land surface gridbox, the ISLSCP LAI is averaged over all 1^o by 1^o gridpoints where the landcover class corresponds to the particular PFT (e.g. broadleaf deciduous forest, broadleaf evergreen forest, or high latitude deciduous forest land cover classes for broadleaf tree PFT) to generate a LAI annual cycle for that PFT in that model gridbox. If no landcover points relevant to a particular PFT are encountered within the model gridbox, then the search for appropriate landcover points is expanded, more longitudinally than latitudinally, until appropriate landcover points are located. In this manner, a LAI annual cycle is determined for each PFT in each model gridbox. In general, when the PFT fractional coverage in a model gridbox is significant, the search for relevant landcover points is successful within 10^o of longitude and 5^o of latitude of the original gridbox location, ensuring that the LAI_{PFT} is reasonable for that region both in terms of amplitude and phase. Based on the LAI annual cycle on each PFT, an annual cycle for all the physical characteristics of vegetation that are thought to be relevant to the surface climate can be derived, including canopy height, surface roughness, canopy water capacity, and canopy heat capacity.

An effort has also been made to represent the observed surface albedo annual cycle, which is partly related to the vegetation annual cycle and partly related to soil moisture fraction in the top soil layer. Annual mean surface albedo biases and errors in the surface albedo annual cycle can be reduced by recalculating the soil albedo and introducing a soil moisture dependence to the soil albedo. A new soil albedo field is derived by assuming that the soil albedo is approximately equivalent to the observed surface albedo when LAI is at its annual minimum. This assumption is invalid in areas where significant vegetation cover is persistent throughout the year, such as in the tropical rainforest regions. However, in these regions, soil albedo essentially is irrelevant due to the extensive vegetation cover. In regions where the observed surface albedo at minimum LAI is contaminated by snow cover (northern hemisphere high latitudes), the standard soil albedo is retained. A recalculation of the surface albedo with the new soil albedo shows that using the newly derived soil albedo helps correct some of the mean biases, but notable biases remain, particularly with respect to the annual cycle. We found that the annual cycle of albedo can be improved by incorporating a linear soil moisture dependence on soil albedo, $\alpha_{soil} = \alpha_{soil}(6 - 2USMF_1)/5$, where $USMF_1$ is the unfrozen soil moisture fraction in the top soil layer. The new surface albedo representation (Figure 10.1) significantly reduces biases in tropical and sub-tropical annual mean surface albedo and improves the representation of the surface albedo annual cycle.

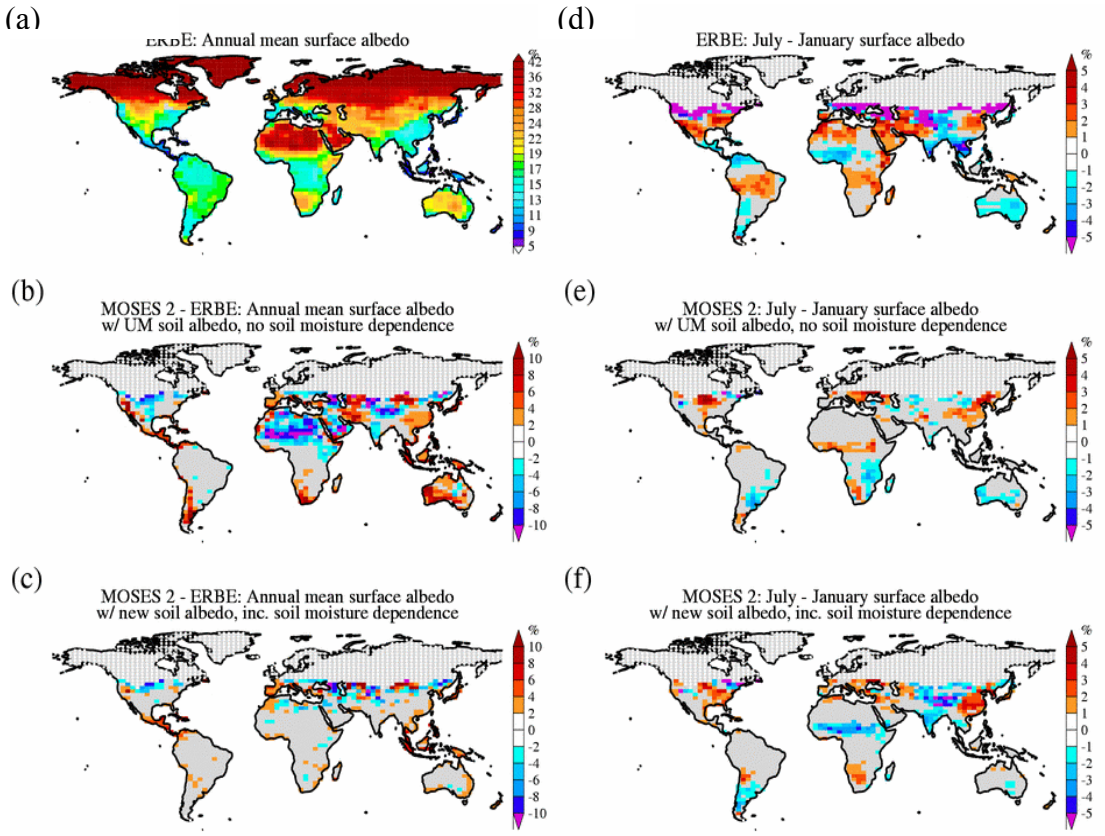

Figure 10.1: Comparison of the annual mean and July-January differences in surface albedo with the albedo estimates from ERBE.

The impact of the annual cycle of vegetation on the climate has been diagnosed from two 25-yr model runs with climatological SSTs are compared. In the first run, annual mean LAI values are imposed throughout the year (LAIMEAN), while in the second run the LAI varies according the observed climatological LAI annual cycle (LAIPHEN). Initial model experiments run both with and without a vegetation annual cycle revealed that a larger LAI does not lead to enhanced evapotranspiration except under low surface soil moisture conditions (Fig. 10.2). Further analysis showed that evapotranspiration is unrealistically independent of LAI (see Fig. 10.2), leading to a relatively weak impact of the vegetation annual cycle on surface climate.

Significant effort has been made to diagnose the problem and to improve the model response to variations in LAI. It was found that two model parameters, k_{par} and k_{shade}, can be adjusted so that the evapotranspiration versus LAI curve more closely follows observed relationships. The insensitivity of the model to LAI is illustrated clearly in plots of surface conductance, $g_s = g_l(1 - e^{-k_{par} LAI}) / k_{par} + e^{-k_{shade} LAI} g_{soil}$, against LAI (Fig. 10.3, top panels blue line). The solid lines in the top panels show the relationship between total surface conductance and LAI for a wet surface g_{soil}= 22 mm s^{-1} for standard MOSES2 k_{par} and k_{shade} parameter values, two evaporation parameters that control transpiration and soil evaporation, respectively. Curves are shown for leaf conductances of 4 mm s^{-1} and 12 mm s^{-1} so that a direct comparison can be made with results from a detailed theoretical surface conductance model (Schultz et al 1995, see their Fig. 2, reproduced and shown as dash-dot lines here). At low leaf conductance, the surface conductance monotonically decreases with LAI so that the surface conductance at large LAI is always less than the surface conductance at small

LAI. In the high leaf conductance case, the surface conductance is nearly the same for all LAI.

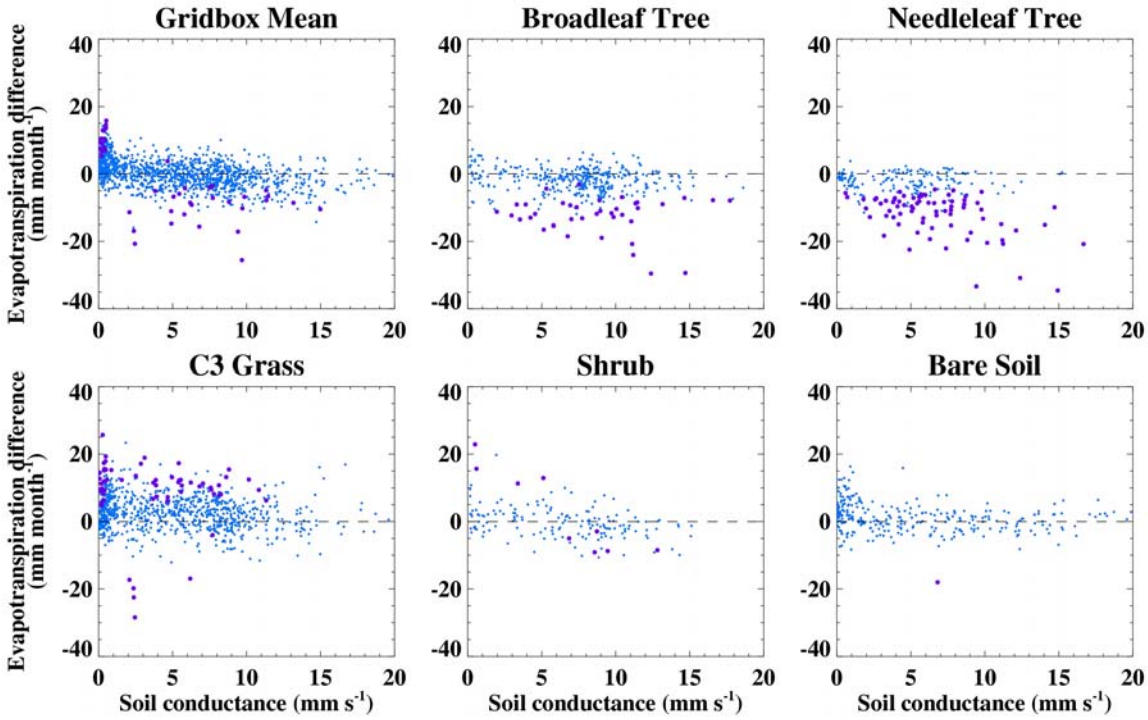

Figure 10.2. Scatter diagrams of summer leaf mean monthly LAIPHEN - LAIMEAN evapotranspiration difference versus soil conductance. All PFTs and the bare soil tile are shown. Only points where and when $LAI_{PHEN} - LAI_{MEAN} > 0.75$ (summer leaf), fractional coverage is greater than 20%, and g_{soil} is within 0.5 mm s^{-1} between runs. Large purple dots are used when difference is statistically significant at 95% level.

The MOSES2 surface conductance curves do not bear much resemblance to those of Schulze et al. (1994). In the Schulze et al. model, surface conductance initially decreases to a minimum value at around LAI equal to 1.5. This minimum is due to reduction of soil evaporation by canopy shading of the soil surface. As LAI increases above 1.5, surface conductance rises asymptotically with LAI to a maximum value that is determined by the leaf conductance. MOSES2 does not capture either the minimum surface conductance at low LAI or the subsequent increase in surface conductance for larger LAI.

We found that the Schulze et al. surface conductance-LAI relationship could be reproduced by adjusting two MOSES2 evaporation parameters, k_{par} and k_{shade} (see curves for different sets of these parameters in Fig. 10.3). Increasing k_{shade} from 0.5 to 1.0, which effectively decreases the fraction of the surface that is directly exposed to the atmosphere and therefore reduces the contribution of soil evaporation to total evapotranspiration under a dense canopy, improves the MOSES2 response by replicating the surface conductance minimum at low LAI, but does not improve surface conductance simulation at high LAI. The extent that surface conductance increases with LAI in MOSES2 is controlled by k_{par}. Decreasing k_{par} from 0.5 to 0.3, which is equivalent to increasing the fraction of light absorbed by the canopy, increases surface conductance at large LAI and brings the MOSES2 surface conductance-LAI relationship into agreement with Schulze et al. (1994).

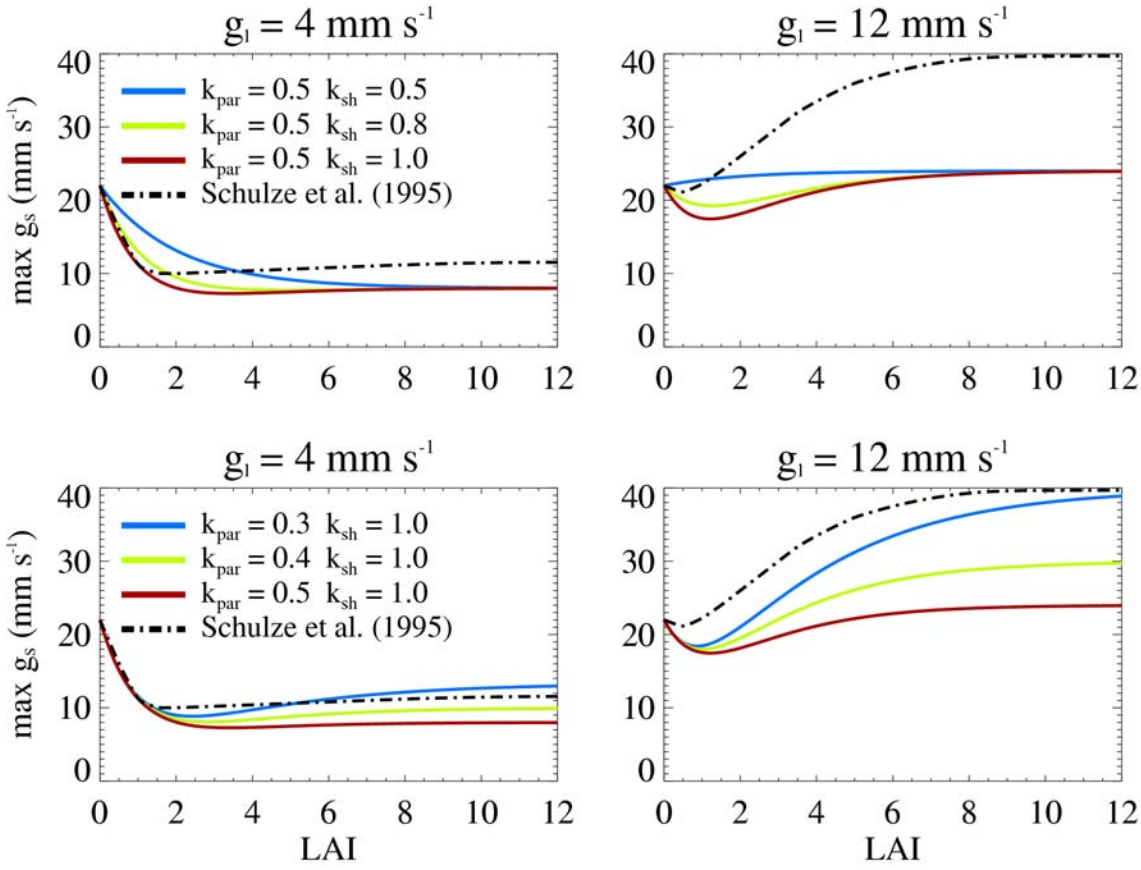

Figure 10.3: Surface conductance (g_s) versus LAI for two leaf conductances (g_l) (4 mm/s, top panels; 12 mm/s, bottom panels) and various sets of k_{par} and k_{shade} parameters. Also shown is surface conductance versus LAI for theoretical results of Schulze et al. (1994). Original model parameters are k_{par} = 0.5 and k_{shade} = 0.5. Adjusted model parameters are k_{par} = 0.3 and k_{shade} = 1.0.

When the same two model experiments are repeated with the adjusted evaporation model parameters, it is found that climate diagnostics such as temperature and evaporation are significantly impacted by an annual cycle of vegetation (Figure 10.4), although precipitation remains notably less affected. Summer leaf evaporation is stronger in the LAIPHEN experiment in nearly all regions, leading to lower surface temperatures through a reduction in the Bowen ratio. During winter, evaporation in the Tropics is reduced when leaf area is small and therefore winter surface temperatures are slightly higher. In the mid- and high-latitudes, the surface temperatures are somewhat lower in the phenology run due to a higher surface albedo over areas of low LAI. The surface and sub-surface hydrology is also significantly impacted, especially in seasonally arid regions. Much of the variations in hydrology are due to reduced evaporation in winter in the phenology run which maintains the sub-surface soil moisture further into the spring and summer seasons leading to enhanced summer sub-surface runoff. Variations in surface roughness and LAI leading to changes in evapotranspiration appear to be the most important factors determining the influence of the annual cycle of vegetation on climate.

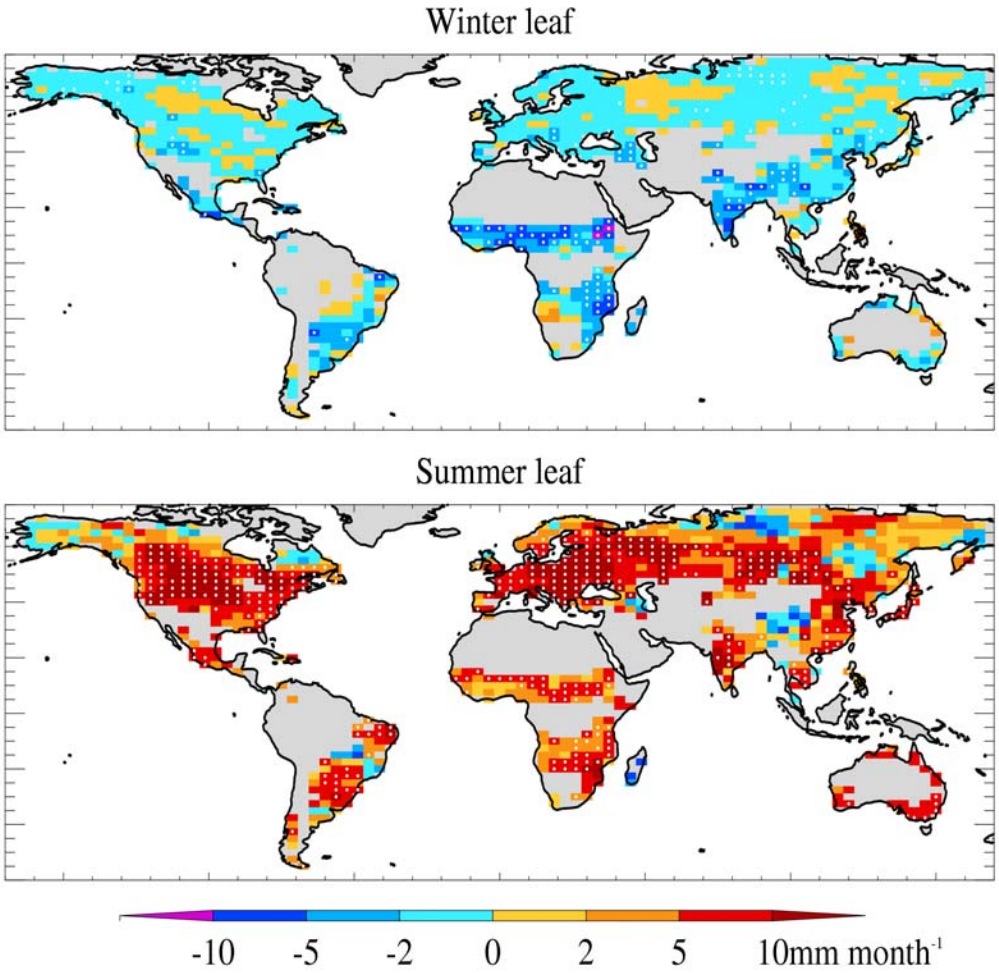

Figure 10.4: Total evaporation difference between LAIPHEN and LAIMEAN runs. Data averaged over months of leaf season, which are defined as winter leaf (LAI_{PHEN} -LAI_{MEAN} < -0.75) and summer leaf (LAI_{PHEN}-LAI_{MEAN} > 0.75). Difference is plotted only if at least one month matches leaf season criteria and gridpoint has an annual cycle in LAI > 1.5. White dots signify gridpoints where the difference is statistically significant at the 95% level.

References:

Lawrence, D.M. and J.M. Slingo, 2003a: A realistic annual cycle of vegetation in a GCM. Part I: Implementation and impact on evaporation. Submitted to *Climate Dynamics*

Lawrence, D.M. and J.M. Slingo, 2003b: A realistic annual cycle of vegetation in a GCM. Part II: Hydrologic and surface energy budgets. Submitted to *Climate Dynamics*

Schulze E.-D., and others, 1994: Relationships among maximum stomatal conductance, ecosystem surface conductance, carbon assimilation rate, and plant nitrogen nutrition. *Annual Rev. Ecol. Syst*., **25**, 629-660.

11. Influence of soil properties on mean climate and response to land cover change: Tom Osborne, Dave Lawrence

As part of our research into the role of vegetation seasonality on surface climate, we have explored the sensitivity of the surface climate to soil parameterization (Osborne et al. 2003).

Chris Taylor at CEH has developed a soil parameterization dataset based on IGBP satellite information. This soil parameterization represents a considerably different, but realistic, representation of soil properties compared to the standard MOSES soil parameterization.

Annual mean differences for soil moisture fraction, surface temperature, precipitation, and sub-surface runoff are shown in Figure 11.1. In general, the IGBP soil dataset generates much drier soils throughout the column, leading to reduced surface evaporation and higher surface temperatures. Annual mean precipitation is relatively unaffected, except for a few areas including northern South America, which exhibits an interesting east-west difference pattern that is strongest in JJA. The cause of this dipolar precipitation difference is not clear, but appears to be associated with enhanced easterly winds across the northeast coastline and enhanced northerly winds during June and July.

Significant enhancement of sub-surface runoff is seen throughout the Tropics, even though precipitation differences over land are relatively small. This enhancement of sub-surface runoff and the drying of the soils in the IGBP soil runs are due to enhanced infiltration through the soil profile.

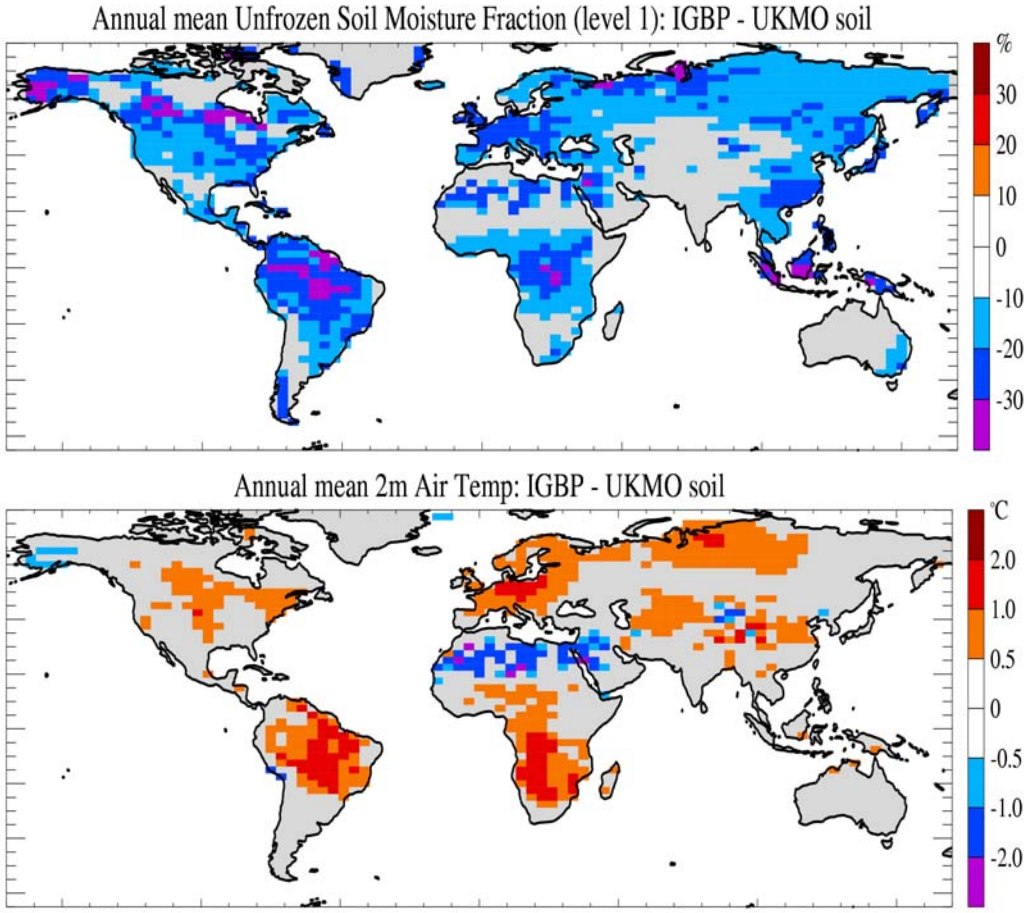

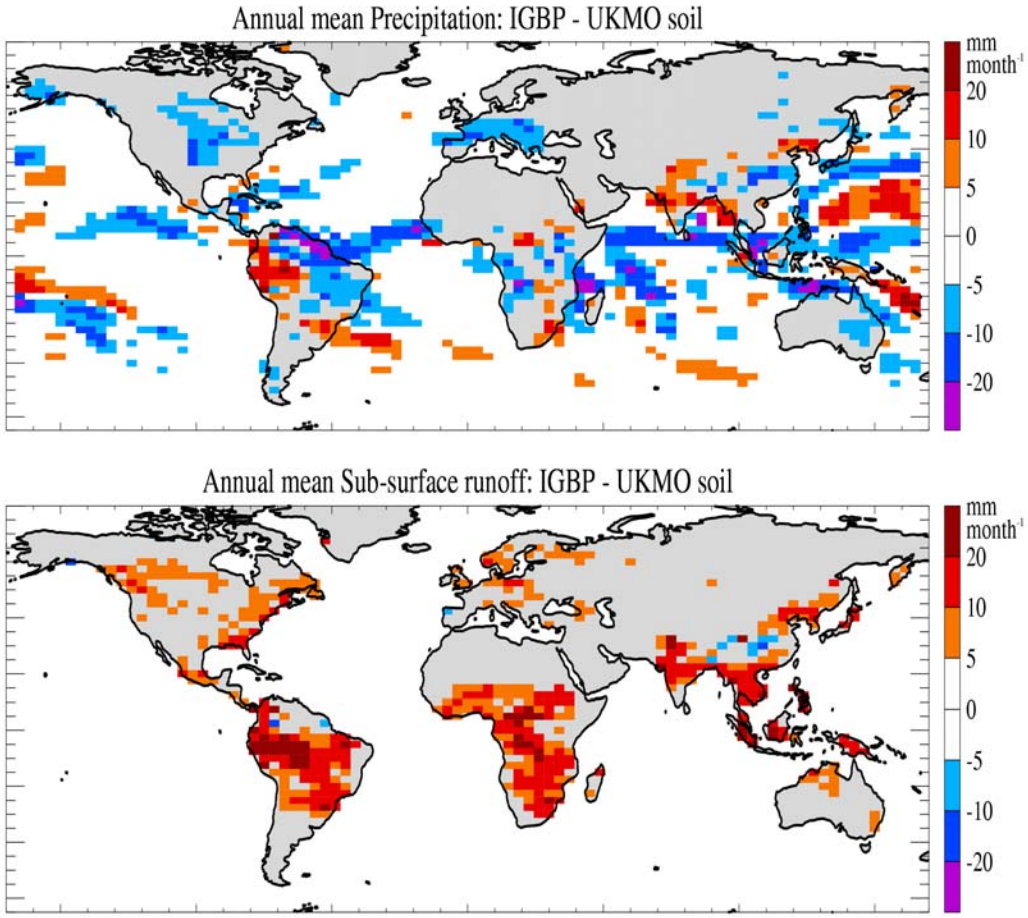

Figure 11.1: Differences for four annual mean model diagnostics for run with IGBP soil parameters compared to the standard MOSES soil parameters (UKMO soil).

Figure 11.2 compares the annual cycle for assorted surface diagnostics between the two soil runs. The wetter soils in the UKMO experiment leads to higher soil moisture availability, evaporation efficiency, total surface conductance, and soil conductance throughout the year. An interesting result is that the change in evaporation efficiency in response to a precipitation event, which is some measure of the land-atmosphere coupling strength, exhibits an interesting annual cycle. During the spring and winter, the change in evaporation efficiency is nearly the same for both soil datasets, but during the summer, the UKMO soil dataset results in significantly greater changes in evaporation efficiency by comparison to the IGBP soil dataset. The reasons for these difference responses are not understood and will be the subject of future investigations.

A sensitivity experiment was conducted where 'tropical vegetation' was removed from the standard MOSES distribution. The experiment was first conducted with the UKMO soils and then repeated with the IGBP soils discussed above. The temperature response to de-vegetation of the tropics is shown in Figure 11.3. In both experiments, the general response is a warmer surface by up to 3^{o} C. However, the response is significantly larger with the UKMO soils dataset due to a greater impact on surface evaporation rates. This is due to two factors. First, the IGBP soils, as noted above, are considerably drier than their UKMO counterparts resulting in lower rates of evaporation in the IGBP control climate and a smaller reduction in evaporation under the de-vegetation scenario. Second, in the de-vegetation experiments, surface evaporation in de-vegetated regions is entirely from the surface soil layer. Assuming

similar surface soil moisture fractions, θ_1, the conductance to soil evaporation (g_{soil}) is greater with the IGBP soil parameterisations, due to a smaller θ_c, the critical soil moisture content below which evaporation falls below the potential evaporation (see equation 11.1).

$$g_{soil} = 0.01 * \left(\frac{\theta_1}{\theta_c} \right)^2 \qquad 11.1$$

In summary, the introduction of more freely draining soils, in the IGBP soils dataset, has changed the soil moisture contents of the control, vegetated system and has reduced, significantly, the climate sensitivity to vegetation and by implication, land use change. Changes to the soil parameters have also had an impact on the soil hydrology and its interaction with vegetation, by altering the partitioning between fast and slow runoff processes. These results raise important questions about the representation of highly heterogeneous soil characteristics in climate models, as well as the potential influence of land use change on the soil characteristics themselves. Further details of the tropical de-vegetation experiments can be found in Osborne et al. (2003).

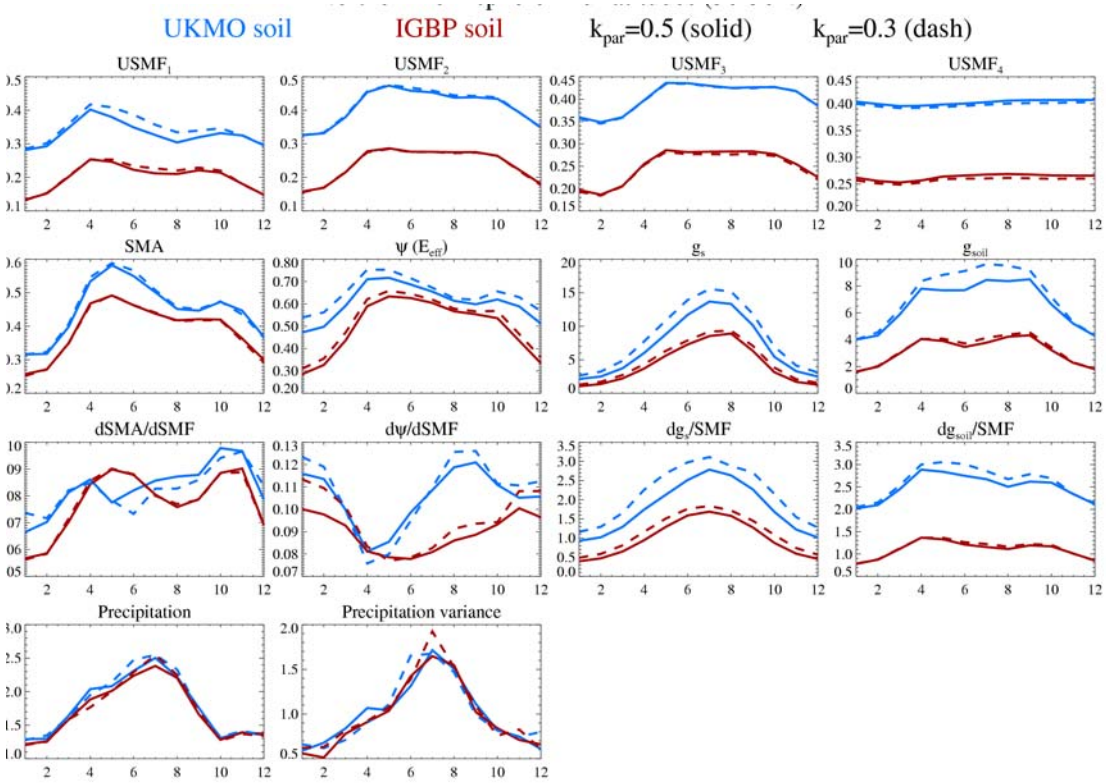

Figure 11.2: Annual cycle curves for assorted surface diagnostics averaged over land areas in northern hemisphere midlatitudes (30^o – 50^o N) for UKMO and IGBP soils. Annual cycles are shown for unfrozen soil moisture concentration (USMF) for each of the four soil levels, integrated soil moisture availability factor (SMA), evaporation efficiency (Ψ), total surface conductance (g_s), soil conductance (g_{soil}), the change in SMA, Ψ, g_s, and g_{soil} associated with soil moisture fraction changes associated with a "typical" 15 mm/day rainfall event, precipitation, and interannual

precipitation variance. Solid lines are for runs using standard model evaporation parameters. Dashed lines are for runs using adjusted model evaporation parameters as described in previous section.

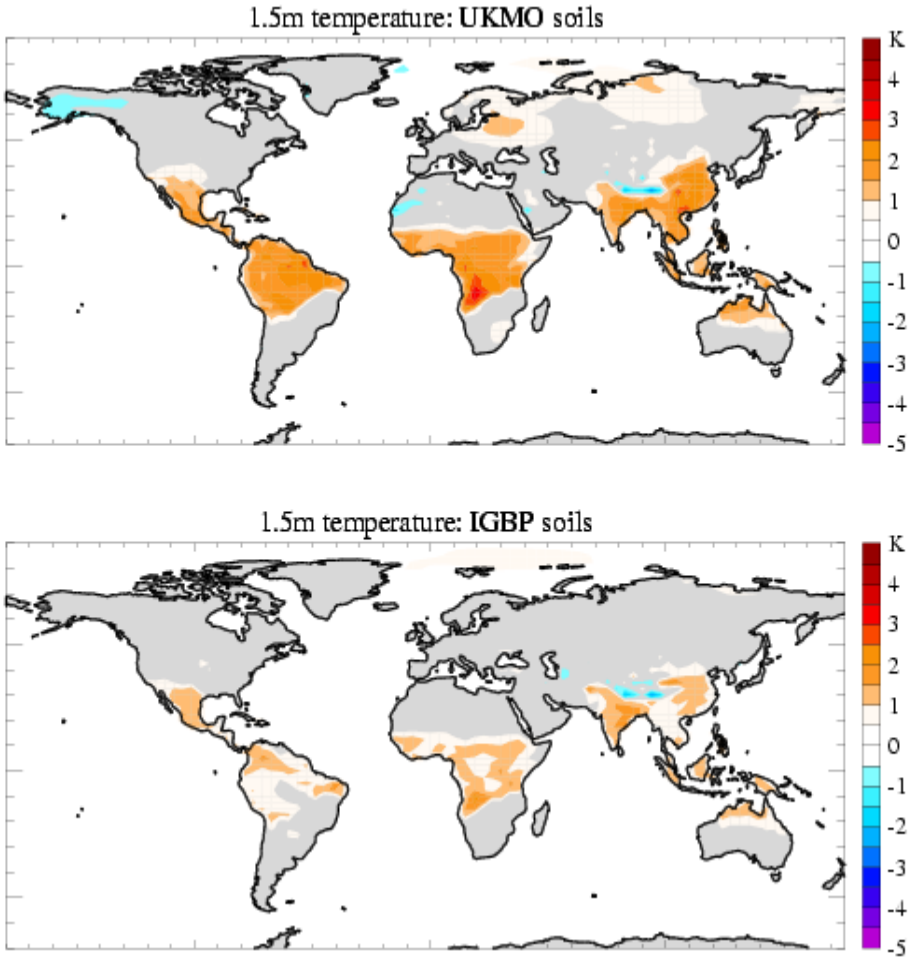

Figure 11.3. Effect of removing tropical vegetation (Expt – Ctrl) on annual mean surface air temperature in HadAM3 with the standard UKMO soils (top) and the 'new' IGBP soil dataset (bottom).

References:

Osborne, T. M., D. M. Lawrence, J. M. Slingo, A. J. Challinor and T. R. Wheeler, 2003: Influence of vegetation on the local climate and hydrology in the Tropics: Sensitivity to soil parameters. Submitted to *Climate Dynamics*.